Rock Size-frequency Distributions of the InSight Landing Site, Mars

M. P. Golombek[1], A. Trussell[1,2], N. Williams[1], C. Charalambous[3], H. Abarca[1], N. H. Warner[4], M. Deahn[4], M. Trautman[1], R. Crocco[1], J. A. Grant[5], E. Hauber[6] and R. Deen[1],

[1]Jet Propulsion Laboratory, California Institute of Technology, Pasadena, CA,

[2]California Institute of Technology, Pasadena, CA,

[3]Imperial College, London,

[4]SUNY Geneseo, Geneseo, NY,

[5]Center for Earth and Planetary Studies, National Air and Space Museum, Smithsonian Institution, 6th at Independence SW, Washington, DC

[6]German Aerospace Center (DLR), Berlin.

Submitted to
Earth and Space Science
7/29/21
v. 4

Abstract

Rocks around the InSight lander were measured in lander orthoimages of the near field (<10 m), in panoramas of the far field (<40 m), and in a high-resolution orbital image around the lander (1 km^2). The cumulative fractional area versus diameter size-frequency distributions for four areas in the near field fall on exponential model curves used for estimating hazards for landing spacecraft. The rock abundance varies in the near field from 0.6% for the sand and pebble rich area to the east within *Homestead hollow*, to ~3-5% for the progressively rockier areas to the south, north and west. The rock abundance of the entire near field is just over 3%, which falls between that at the Phoenix (2%) and Spirit (5%) landing sites. Rocks in the far field (<40 m) that could be identified in both the surface panorama and a high-resolution orbital image fall on the same exponential model curve as the average near field rocks. Rocks measured in a high-resolution orbital image (27.5 cm/pixel) within ~500 m of the lander that includes several rocky ejecta craters fall on 4-5% exponential model curves, similar to the northern and western near field areas. As a result, the rock abundances observed from orbit falls on the same exponential model rock abundance curves as those viewed from the surface. These rock abundance measurements around the lander are consistent with thermal imaging estimates over larger pixel areas as well as expectations from fragmentation theory of an impacted Amazonian/Hesperian lava flow.

Key Points

Rocks measured within 10 m, 40 m and ~500 m of the InSight lander cover 0.6-5%, ~3% and 4-5% cumulative fractional area of the surface.

The rock size-frequency distributions observed from orbit and the surface are on similar exponential model curves.

Rock abundance at InSight is between the Phoenix and Spirit landing sites and is consistent with orbital thermal imaging estimates.

1. Introduction

The size-frequency distribution (SFD) of rocks on Mars is important for understanding the geologic and geomorphic history of the surface (e.g., Garvin et al. 1981; Ward et al. 2005; Yingst et al. 2007, 2010, 2013, 2016; Grant et al. 2006; Craddock and Golombek, 2016), for determining the aerodynamic roughness important for eolian processes (Hébrard et al, 2012; Charalambous et al., 2020), for quantifying the hazards for landing spacecraft (Golombek and Rapp, 1997; Golombek, Haldemann et al., 2003, Golombek et al., 2008, Golombek, Huertas et al., 2012), and for evaluating the trafficability for roving (Golombek, Grant et al., 2012, Golombek, Otero et al., 2017). In this regard, rocks are defined as naturally occurring solid masses on the surface that are distinct from finer grained soils. Rock counts have been made by all the landers or rovers on the surface of Mars and they have been related to various functions to

fit their size-frequency distributions (SFD). Initially power law distributions were used to fit measured Viking lander rock distributions (Binder et al., 1977; Moore et al, 1979) and single fragmentation events are expected to be fractal and scale invariant and so can be represented by a power law (Turcotte, 1997). Although power laws do reasonably fit portions of rock size-frequency distributions, which show up as straight lines when plotted on log-log plots of the cumulative number of rocks (normalized by area) versus rock diameter, they invariably overestimate the number (or area) covered by large and small rocks. In addition, power laws must have defined size ranges over which they are valid. Exponential models of the cumulative fractional area versus diameter of rocks at the Mars landing sites avoided the overestimation of large rocks and small particles (Golombek and Rapp, 1997) and are generally similar to Rosin Rammler and Weibull distributions that have also been used previously to describe rock populations (Rosin and Rammler, 1933; Gilvarry, 1961; Gilvarry and Bergstrom, 1961), which predicts that ubiquitous flaws or joints will lead to exponentially fewer blocks with increasing size during weathering and transport (e.g., Wohletz et al. 1989; Brown and Wohletz 1995).

The advent of High-Resolution Imaging Science Experiment (HiRISE) images at ~30 cm/pixel showed that the SFD of rocks >1.5 m diameter measured from orbit and smaller rocks from the surfaces of landing sites fall on the same exponential model curve (Golombek et al., 2008, Golombek, Huertas et al., 2012). These observations support the use of HiRISE images to measure rocks >1.5 m diameter, fitting these rocks to an exponential SFD model, and extrapolating along the model to predict the number of rocks smaller than 1.5 m that could be potentially hazardous to landing spacecraft Golombek et al., 2008; Golombek, Grant et al., 2012; Golombek, Huertas et al., 2012; Golombek, Kipp et al., 2017; Golombek, Otero et al., 2017). These fits also show that the lognormal models for the rock size-frequency distributions on Mars

proposed by Hébrard et al. (2012) to derive an aerodynamic roughness map for atmospheric and eolian studies severely underestimate the number or area covered by large rocks (Golombek, Huertas et al., 2012). The exponential model equations are of the form: $F_k(D) = k \exp [-q(k) D]$, where $F_k(D)$ is the cumulative fractional area (CFA) covered by rocks of diameter D or larger, k is the fraction of the total area covered by all rocks, and an exponential $q(k)$ that governs how abruptly the fraction of the total area covered by rocks decreases with increasing diameter (Golombek and Rapp 1997), which is approximated by $q(k) = 1.79 + 0.152/k$. These distributions form a family of non-crossing curves that flatten out at small rock diameter. Note that these models are based on the area covered by rocks (diameter squared), which when translated into cumulative number per m^2 distributions by numerical integration on a log-log plot results in a less curved distribution than a true exponential (e.g., Golombek, Haldemann et al. 2003, 2008, Golombek, Huertas et al., 2012; Craddock and Golombek, 2016) that can be fit more readily to power law distributions over a limited diameter range (e.g., Grant et al. 2006; Russell et al. 2013).

Charalambous (2014) has shown that repeated fragmentation events, each of which is scale invariant (fractal) or a power law (Turcotte, 1997), results in a particle size-frequency distribution described by a negative binomial (NB) function that resembles the exponential models. Rock counts in nearly complete HiRISE coverage of the InSight landing site, were fit by a NB function and predicted by the observed cratering (Golombek, Kipp et al., 2017) and resulted in simulated surface and subsurface rock distributions that are consistent with observations at the surface (Charalambous et al., 2019; Golombek, Kass et al., 2020). Finally, a composite size-frequency distribution of particles (rocks to dust) can be explained by fragmentation due to impact for particles above 0.2–0.5 mm, with eolian activity responsible for

129 the reduction below this size; together these processes can produce the global surface layer of
130 mostly sand sized particles on Mars (Golombek, Charalambous et al., 2018, 2020).

131 The InSight mission (Interior Exploration using Seismic Investigations, Geodesy, and
132 Heat Transport) landed in November 2018 and has acquired a number of panoramas (Golombek,
133 Warner et al., 2020) using an arm mounted color camera (Instrument Deployment Camera, IDC,
134 Maki et al., 2018) with stereo images that have been made into a nearly complete digital
135 elevation model (DEM) and orthomosaic. InSight landed in western Elysium Planitia within a
136 quasi-circular depression, interpreted to be a ~27 m diameter, degraded impact crater (Warner et
137 al., 2020), informally named *Homestead hollow*, with a smooth pebble-rich surface adjacent to a
138 slightly rockier and rougher terrain (Golombek, Warner et al., 2020). The broader surface
139 appears modified by impact, eolian and lesser mass wasting processes with craters in various
140 stages of degradation (Golombek, Warner et al., 2020).

141 Prior to landing, orbital estimates of rock abundance in the landing ellipse indicated a
142 surface with very low average rock abundance (Golombek, Kipp et al., 2017). In HiRISE, the
143 average cumulative fractional area (CFA) covered by rocks is ~1-2% away from craters with
144 obvious rocks in their ejecta (so called rocky ejecta craters). Using all rocks within the ellipse,
145 including sparse rocky ejecta craters, yields a CFA of ~6%. These low rock abundances are
146 consistent with thermal imaging estimates of rock abundance (<5%) and are generally
147 comparable with rock distributions measured at the Phoenix and Spirit landing sites (Golombek,
148 Kipp et al., 2017).

149 After landing, initial rock counts were performed in a number of small (1-7 m^2) areas
150 around the lander that had stereo coverage (Golombek, Warner et al., 2020, Golombek, Kass et
151 al., 2020). These counts showed surfaces with rock abundance of 1-4% that were generally

similar to and bounded by the rock abundances at the Phoenix and Spirit landing sites. This paper, presents the rock counts and SFD in the nearly complete DEM panorama, which covers more area (~200 m^2) and is a better representation of the rock population around the lander. We also measured rocks that can be identified in both a HiRISE image and surface panorama in the far field, extending out to ~40 m from the lander. In addition, the largest individual rocks as well as distributions around the lander are compared to rocks measured in the area around the lander in HiRISE. Results indicate that the >1.5 m diameter rocks measured in HiRISE images fall on the same exponential model curves as those measured on the ground and that the SFD is well represented by exponential model curves for CFAs of 1-5%. We begin with rocks measured around the lander in the panorama orthoimage and discuss their SFD. Next, we measure rocks in the far field that can be seen in InSight and HiRISE images, derive their SFD and compare the largest ones to those measured in HiRISE. We present the HiRISE rock SFD in a km size area around the lander and compare the results from those acquired from the lander and discuss their implications for Mars rock SFDs and fragmentation theory.

2. Near Field Rock Distributions

2.1. Panorama DEM and Orthomosaic

IDC stereo images (N=283) acquired on Sols 12-160 were mosaicked to create a panorama DEM and the orthoimage shown in Figure 1. The images for the DEM were acquired in 5 sections with vertical and horizontal stereo offsets to fill in the 360° as well as the upper right quadrant of all images where the arm obstructs the terrain. Image scale varied from 0.12 cm/pixel to 2.8 cm/pixel with increasing distance and the DEM has elevation postings every 5 mm. The panorama orthomosaic has been bundle adjusted (Abarca et al., 2019), except for the west region, which does not overlap with the rest of the panorama. Stereo coordinates have

multiple sources of error stemming from the robotic arm position uncertainty and stereo processing errors (from stereo range and camera model errors). During pre-launch testing, error analysis and stereo processing was focused on the workspace region in front of the lander where the instruments were to be deployed by the robotic arm. Tests showed the workspace DEM had a mean horizontal accuracy of 11 mm, a mean absolute vertical accuracy of 6.5 mm, and mean relative vertical accuracy of 5 mm. After landing, the sol 12 workspace images (N=56) in front of the lander had a spatial accuracy between adjacent stereo frames of 1.9 mm overall with a maximum error between frames of 4 mm. Images beyond the workspace, including horizon images, were bundle adjusted to those in the workspace. Arm uncertainty increases when the robotic arm is positioned to image the horizon due to the motions that are required to reach the imaging poses. The arm uncertainty and minimal overlap between frames led to large vertical seams 10 cm wide between the 3 sections of the panorama DEM, and up to 25 cm behind the lander. The error within each stereo pair, however, is characterized by the stereo range error (Maki et al., 2018) of the IDC camera. Range error in the DEM spans from 9 mm closest to the rover in the workspace to roughly 13 cm at the 10 m range. The position of the IDC images when they were acquired was in the IDA (Instrument Deployment Arm) robotic arm frame and were translated to the Site Frame (positive north and east coordinates), which corrects for spacecraft tilt and orientation provided by the inertial measurement unit (IMU). Comparison of azimuths to features identified in both the surface, controlled panorama and a hierarchically georeferenced HiRISE orthoimage of the landing site shows azimuths agree to <1°, which is the expected to accuracy of the IMU (Golombek, Williams et al., 2020).

2.2. Method

The orthomosiac and DEM were divided into four subareas in the north, south, east, and west directions (Figure 1). Because InSight is on a shallow slope down to the east (Golombek, Williams et al., 2020), stereo definition is more limited in distance in this direction than others (Figure 1). Rocks larger than 0.01 m were measured by digitizing polygonal outlines of visible rocks in the orthomosiac in ArcGIS Pro. A convex hull was calculated providing minimum and maximum (non-vertical) axes that enclosed the entire rock. The minimum axis is calculated as the shortest distance between any 2 vertices of the minimum bounding polygon while the maximum axis is calculated as the longest distance between any 2 vertices of the minimum bounding polygon. Measurements in the orthomosaic are exactly horizontal with no elevation information. These two axes were averaged to yield an average rock diameter in meters. The area of each quadrant was calculated by drawing a polygonal shape around the edges of each visible mapping space, which excluded gaps in the orthomosaic (Table 1). Size-frequency distributions were then calculated for each region over its given area. All measurements and areas were then combined to give a size-frequency distribution for all rocks in the orthomosaic. The four areas measured range from 31 m^2 to 65 m^2 and included 90-1160 rocks. The total area is 207.3 m^2 and the total number of rocks counted is 2017; the total number of rocks >3 cm diameter is 854. The size-frequency distributions are reported for rocks >3 cm diameter and are shown on log-log plots. Although spatial uncertainties in the orthomosaic of <4 mm in the workspace to <1 cm at 10 m distance are estimated, uncertainties in the measurements of rocks over small distances within the orthomosaic are much less and do not have an appreciable effect on the rock measurements.

2.3. Size-frequency Distributions

The near field size-frequency distribution of CFA versus diameter or rock abundance around the InSight lander varies from <1% to ~5% (Figure 2). The least rocky, smooth plains surface of *Homestead hollow* to the east of the lander, falls on a model SFD curve for 0.6% CFA. The SFD of the highest rock abundance area to the west of the lander falls on a model 5% CFA for diameters <10 cm, but drops to just over the ~2% model curve for larger diameters. The SFD of the area to the north includes the largest rock counted (44 cm) and rises from ~3% CFA for the largest rocks to ~4.5% for diameters <30 cm. The area to the south of the lander rises from ~1% CFA at 20 cm diameter to just below 3% CFA for diameters <10 cm. The SFDs of all areas are generally parallel to the exponential model curves at diameters <10-30 cm. All areas, except the area to the east, fall below the models for larger diameters, indicating a relative deficiency of large rocks. The entire area together has a SFD that is close to the exponential 3% model curve for diameters <30 cm and a 3.4% model curve for rocks smaller than 0.15 m.

These SFDs are generally similar to initial counts obtained over smaller areas (Golombek, Warner et al., 2020; Golombek, Williams et al., 2020), except the range in rock abundance is greater and the SFDs are clearly curved on the log-log plot and more closely resemble the curved exponential model SFDs than the initial smaller area counts, some of which approximated power laws (straight lines). *Homestead hollow* has the lowest rock abundance (0.6%) and the area to the north and west have the highest (4-5%). The lower rock abundance within the hollow likely reflects a real paucity of rocks within the fill as compared to exterior surfaces due to more significant burial by infilling sediments (Grant et al., 2020). The average rock abundance for the entire area counted is ~3%, which is between the ~2% at the Phoenix and 5% at the Spirit landing sites. The rockier areas to the north and west (4-5%) are more representative of the area around the lander that includes rocky ejecta craters (Golombek, Kass et

247 al., 2020), compared with the rock-poor area of *Homestead hollow*. The rockier area to the west,
248 could also be due to rays of ejecta from younger nearby craters (Grant et al., 2020).

249 The cumulative number of rocks (per m^2) larger than any given diameter versus diameter
250 plot for the four areas and total SFD indicate generally similar total rock abundances with some
251 subtle differences (Figure 3). The model curves in this plot are less curved than in CFA plots,
252 because they are numerically integrated from the exponential CFA models where the area is the
253 diameter squared, versus the cumulative number (diameter not squared). The cumulative number
254 SFD of the area to the east of the lander in *Homestead hollow* also falls on the 0.6% model
255 curve. The SFD of the area to the west of the lander rises from about the 3% model curve for
256 rock diameter of 0.3 m to about 5% for rock diameter of <0.2 m. At diameters below 0.2 m, the
257 west SFD is between the 5% and 10% model curves before decreasing to ~3% at 0.03 m. The
258 shape of the SFDs for the areas to the south, north and total are similarly more curved than the
259 model distributions with fewer rocks at large and small diameters compared with intermediate
260 diameters. In addition, the intermediate cumulative number SFDs for the areas to the south and
261 north are parallel to model curves with slightly higher CFA than the CFA SFD plots in Figure 2
262 (area to the south is ~5% and the area to the north is ~6%).

263 The exponential CFA model SFDs were developed for hazard analysis of landing
264 spacecraft on Mars in which large rocks that can damage spacecraft are important. For Mars
265 Pathfinder, Mars Exploration Rover, Mars Science Laboratory and the Mars 2020 Rover, rocks
266 of concern are about 0.5 m high or ~1 m diameter for hemispherical rocks (Golombek et al.,
267 1997, Golombek, Grant et al., 2003, 2012) and 0.35-0.45 m height or ~0.7-0.9 m diameter for
268 Phoenix and InSight (Arvidson et al., 2008; Golombek, Kipp et al., 2017). Rock SFDs at most of
269 the landing sites reasonably follows the exponential curves down to around 0.03 m diameter

(Figures 4 and 5). However, SFDs at the Phoenix and Spirit landing sites, rocks with diameters <0.06 m have slopes that are steeper than the model SFDs and appear more power law like (straight line on these log-log plot) (Figures 4 and 5). For the plots of InSight rocks, we cut the SFDs off at 0.03 m diameter, but rocks with smaller diameter were measured (Table 1). Rocks smaller than 0.03 m diameter become progressively more difficult to map farther from the lander as the resolution decreases and small rocks are occluded by larger rocks. However, we estimate that we counted 80-95% of all rocks present at that size range to see what happens to the SFD below 0.03 m diameter. In CFA versus diameter plots, all four areas SFDs flatten out at diameters <0.03 m (to 0.02 m). For the cumulative number per m^2 versus diameter plots, the slope of all four areas SFDs is less than the model distributions at 0.02 m diameter. As a result, the InSight rock SFDs do not appear to have steeper slopes than the models similar to the Phoenix and Spirit landing sites. We attribute the power law behavior of the SFD of the workspace counts reported in Golombek, Warner et al. (2020) and Golombek, Williams et al. (2020) to be due to the small areas counted and the limited diameter range (i.e., the lack of large rocks).

The rock SFD of the InSight landing site are generally similar in shape to local rock measurements made at other landing sites on Mars. The shape of the SFD of CFA versus diameter plot of the InSight landing site is generally similar to the other landing sites and the exponential model distributions (Figure 4). Furthermore, the deficit of large rocks counted compared to the models at the InSight landing site is also observed for the Viking Lander 1, Viking Lander 2 and Mars Pathfinder sites even though these sites have higher rock abundances of around 7%, 16% and 19%, respectively (Figure 4). Comparison with the SFD of rocks in HiRISE images for these sites indicates this deficit does not extend to larger diameter (Golombek

et al., 2008; Golombek, Huertas et al., 2012), indicating the effect is due to the generally small areas measured around the landers and the statistics of including larger rocks in these small areas. The InSight landing site rock abundance of ~3% is greater than the Phoenix landing site (~2%) and less than the Spirit landing site (7%), Viking Lander 1 (~7%), the Legacy Spirit site (7%) and the Bonneville Spirit site (~20%). The SFD of the cumulative number per m^2 versus diameter plot of the InSight landing site is also similar in shape to local rock measurements at other landing sites on Mars (Figure 5). In particular, the shape of the rock cumulative number SFDs for InSight are similarly more curved than the model distributions with fewer rocks at large and small diameters compared with intermediate diameters like the SFDs at Viking Lander 1, Viking Lander 2, and Mars Pathfinder even though these sites have higher CFAs. In addition, the cumulative number SFD for InSight is parallel to model curves with higher CFA at intermediate diameters than the CFA SFD (~5%), similar to the intermediate diameter SFDs at Viking Lander 1 (~10%), Viking Lander 2 (20%), Mars Pathfinder (~30%) and Spirit Bonneville (30-40%) (Figure 5).

3. Far Field Rock Distributions

3.1. Far Field Rocks

After InSight landed, craters, rocks and bedforms that could be identified in both the InSight panoramas and in HiRISE were identified (Golombek, Warner et al., 2020, Golombek, Williams et al., 2020). Golombek, Williams et al. (2020) further mapped 11 large rocks and 15 craters (1-10 m diameter) that could be confidently identified in both and included a HiRISE image georeferenced into a map view showing the location of these features out to around 40 m distance from the lander. These same rocks and craters were also identified in eight ~45° views of the surface panorama. The azimuths of these features in the panoramas matched their

azimuths in the HiRISE image to within 1° indicating the spacecraft Inertial Measurement Unit that measured the yaw, pitch and roll of the spacecraft to determine the site frame (with respect to north on Mars) was accurate within 1° as expected (Golombek, Williams et al., 2020). Herein we have identified and mapped a total of 82 rocks that could be identified in both the HiRISE image (Figure 6) and the InSight panoramas (Figures 7-14) so as to better characterize the rock distribution over a broader area (out to ~40 m) from the lander in the orthomosaic. Because these rocks can be identified in the HiRISE image, their distance from the lander could be measured and their diameter and height could be determined from the size of the pixels in the panorama of the IDC at that distance.

3.2. Far Field Rock Method

Relatively large rocks were identified in the afternoon and evening portions of the IDC panoramas that emphasized shadows. The relative distance of the rock was initially estimated qualitatively in the panorama by its position and size with respect to large rocks and craters that had already been identified (Golombek, Williams et al., 2020) (Figures 7-17). The azimuth of the rock was noted in the panorama and then the HiRISE image was inspected for circular to elliptical shadows that extended to the southeast, i.e., the perpendicular to the terminator, separating the illuminated rock face, at the relative distance estimated in the panorama. If a light-dark pattern of pixels (to northwest and southwest, respectively) was identified, the azimuth and relative distance was compared to that in the panorama. Finally, the location of the rock and its size had to match the azimuth (with the shadow extending to the southeast), relative distance and size of other nearby surface features to be considered a match. Once the rock was identified on the HiRISE image, the azimuth and distance from the lander was measured. We used a sharpened, not map projected HiRISE image (NO MAP, ESP_036761_1845) with a pixel

342 resolution of 27.5 cm/pixel to avoid resampling pixels that was georeferenced into a map view
343 (Figure 6).

344 To measure the size of the rocks, the IDC camera pixel scale of 0.82 mrad/pixel at the
345 center of the image (Maki et al., 2018), was multiplied by the distance to the rock in meters to
346 get the size of each pixel in mm. Rock height was measured by counting the number of pixels in
347 a vertical column from the base to the top of the rock. The width of the rock was measured by
348 counting the number of pixels across a horizontal row. The number of pixels was multiplied by
349 the size of each pixel at that distance to get the width and height of each rock. Because the
350 images of the rocks are oblique only the side or sides facing the camera could be seen and so
351 independent measurements of the length and width of the rocks could not be made. However,
352 there is no reason that the orientation of the rocks viewed from the lander would have a preferred
353 direction, so the observed apparent width can be considered as an average sample of the actual
354 rock diameter. This is the same assumption for rock diameter measured from shadows in HiRISE
355 images where the solar illumination direction is constant in the image and thus the measured
356 width of the shadow can be considered an average sample of the rock diameter (e.g., Golombek
357 et al., 2008, Golombek, Huertas et al., 2012). As a result, we will assume that the measured
358 apparent width is roughly the diameter.

359 There are 82 far field rocks measured in this dataset over a total area of 2630.38 m^2
360 (Figures 7-14, Table 2). Rocks measured range from 5-40 m away from the lander. Rock
361 diameter varied from 0.1 m to 0.6 m and rock height varied from 0.1 m to 0.3 m. Roughly a third
362 of the rocks have diameters below the pixel scale of the HiRISE image (~0.3 m/pixel) indicating
363 the signal to noise of the HiRISE camera is sufficient to produce illuminated (bright)-shadow
364 (dark) pairs that are as small as two pixels. In general, far field rocks are higher than the usual

hemisphere of one half the diameter, but this is not surprising as taller rocks are easier to see in distant oblique images and cast longer shadows in HiRISE images.

Uncertainties in the measurements are due to azimuthal uncertainties in the surface panorama, spatial and azimuthal uncertainties in the HiRISE image, and the camera pixel scale. Spatial uncertainties in the HiRISE image and azimuths in the surface panorama probably do not contribute as the HiRISE image was carefully georeferenced to a hierarchically georeferenced suite of decreasing resolution orthoimages and DEMs that control its spatial and azimuthal accuracy and comparisons with the controlled panorama show uncertainties in azimuth to less than 1° (Golombek, Williams et al., 2020 and section 4). These uncertainties are only relevant to identifying the same rock in both images and measuring the distance to the rock and are probably small compared to the camera pixel scale. IDC pixels range in size from 0.5 cm to 3.3 cm from 5 m to 40 m, respectively, so given that rock width and height can only be measured to ±1 pixel (e.g., Golombek et al., 2008), this is the uncertainty in the rock measurements. Far field rocks are greater than 13 cm in diameter, so uncertainties of <3 cm will have no appreciable effect on the log-log plots of size-frequency distributions.

3.3. Far Field Rock Size-Frequency Distribution

The SFD of the CFA versus diameter of rocks in the far field fall around the 3% model curve for diameters of 0.4 m to 0.9 m (Figure 15). At diameters below 0.4 m diameter, the slope of the SFD flattens considerably. This flattening of the SFD is likely due to resolution roll off, where only some rocks of small size, which in this case are below the pixel scale of the HiRISE camera, are detected. This resolution roll off is typical in HiRISE detections of rocks (Golombek et al., 2008, Golombek, Huertas et al., 2012) as well in crater SFDs where the crater diameter

approaches the resolution of the image. The far field CFA SFD peaks just above the 3% model curve at almost the same maximum of ~3.2-3.5% CFA as the SFD of all rocks measured in orthoimages within 10 m of the lander. The cumulative number of rocks per m^2 versus diameter plot for far field rocks also falls on the same model curve as all rocks measured near the lander Figure 16. The similarity of the far field and nearby CFA (just above 3%) indicates that the rock distribution within 10 m of the lander is similar to that within around 40 m of the lander.

4. HiRISE Rock Distributions

During landing site selection, measurements of rocks in >50 HiRISE images derived via the rock machine vision shadow segmentation, analysis, and modeling method used for Phoenix and Mars Science Laboratory landing sites (Golombek et al., 2008, Golombek, Huertas et al., 2012) was used to measure the rocks in the InSight landing ellipse (Golombek, Kipp et al., 2017). Rock diameter and height were measured to ±1 HiRISE pixel (~0.3 cm, Golombek et al., 2008). Maps of rock abundance in 150 m by 150 m square areas (22,500 m^2) show rocks are concentrated around sparse rocky ejecta craters (up to 35% CFA), but is very low in between (1-2%). To compare the rock counts made from orbit to those made from the lander, all rocks detected in a 1 km sided square centered on the lander were plotted. However, because detections include false positives (scarps, hills, eolian bedforms) that were generally >2.25 m diameter, the estimate of rock abundance was based on rocks 1.5-2.25 m diameter (Golombek, Huertas et al., 2012, Golombek, Kipp et al., 2017).

To remove false positives, we selected detections that were confirmed by a human who mapped rocks, craters and eolian bedforms in a HiRISE orthoimage (ESP_036761_1845 at 25 cm/pixel) and the 1 m elevation posting DEM (created from ESP_036761_1845 and

ESP_037262_1845, designated as InSightE17_C by Fergason et al., 2017). A total of 7069 rocks were mapped by human detection within a 2.25 km^2 area surrounding the landing site. Rocks that are >2 to 4 HiRISE pixels in diameter (0.5 cm – 1 m) form obvious, circular to elliptical shadows that extend to the southeast (solar illumination from the northwest at 54° from vertical), in the opposite direction of the illuminated rock face. This illumination pattern is distinguishable from small, meter-size craters that cast arcuate illuminated rims towards the northwest and corresponding shadows to the southeast (if a prominent rim is present). Each identified rock was marked in ArcGIS with a single point based on these criteria. No attempt was made to digitize the areal extent of each rock or measure their diameters. The map area was subdivided into 0.3 km by 0.3 km grids to ensure complete mapping coverage.

The machine vision rock detection algorithm using shadows is performed on non-map projected HiRISE images (NOMAP). Map projected HiRISE images have resampled pixels to a constant 25 cm/pixel, which can blur the edges of shadows. As a result, rock detections based on shadow segmentation in NOMAP images had to be georeferenced to the map projected version of the HiRISE image and the orthophoto used for the human mapping. The NOMAP image (ESP_036761_1845_RED.NOMAP.tif) was georeferenced to the map-projected HiRISE visible image using 66 tie-points and rubber sheet links between the source points in the NOMAP image and the target points in the map-projected HiRISE image. A linear spatial adjustment was performed using these rubber sheet links allowing the rocks to be transformed into the map-projected HiRISE image. After georeferencing, rocks in the HiRISE image were within 0.5 meters of their original location in the NOMAP image. In order to match rock detections in the map-projected HiRISE image, a spatial join was executed by searching within a 1.5 m radius of each rock point. Rock features within a 1.5 m radius of each other were linked as the same rock.

436 Figure 17 shows 3397 rocks mapped by a human and the confirmed machine vision rocks
437 (172). These rocks are between 0.4 m and 2 m in diameter and the majority of them are located
438 around three rocky ejecta craters (Golombek, Kass et al., 2020). Of these, the 100 m diameter
439 Sunrise crater is the freshest and is about 400 m to the east-southeast (Figure 17). Other detected
440 rocks including those around the lander are not obviously related to the rocky ejecta craters
441 (Grant et al., 2020).

442 The SFDs of the confirmed machine vision rocks are plotted in Figures 15 and 16. The
443 CFA versus diameter SFD (Figure 15) for rocks >1.6 m to 2 m diameter is parallel to the 5%
444 exponential model distribution. The CFA SFD for rocks 1.6-1.2 m diameter is parallel to the 4%
445 exponential model distribution. The SFD of rocks smaller than 1.2 m diameter shallows relative
446 to the exponential model curves similar to most HiRISE counts, which is due to resolution roll
447 off in which rocks with fewer than 5 pixels are detected less frequently (Golombek et al., 2008,
448 Golombek, Huertas et al., 2012). The SFDs for the cumulative number of rocks per m^2 (Figure
449 16) show similar relationships.

450 The 4-5% rock abundance indicated by the HiRISE detections from orbit is 1-2% higher
451 than rocks measured near the lander and in the far field. It does match the 4-5% of the rockier
452 areas to the north and west (4-5%) of the lander. Counts of rocks in 150 m square tiles (22,500
453 m^2 area) used to estimate the CFA (Golombek, Kipp et al., 2017), show that although the area
454 within a few hundred meters has low rock abundance (1-2%), rocky ejecta craters within 0.5 km
455 (Figure 17) produce a spike in rock abundance (Golombek, Kass et al., 2020) that appears
456 responsible for the measured 4-5% rock abundance.

457 As a result, the rock abundances observed from orbit falls on similar exponential model
458 rock abundance curves as those viewed from the surface. Therefore, InSight joins Viking Lander

2, Mars Pathfinder, Phoenix and Spirit landing sites where rock counts in HiRISE images fall on the same exponential model curve as those seen from the surface (Golombek et al., 2008, Golombek, Huertas et al., 2012). The measurements further strengthen the use of HiRISE images to measure rocks >1.5 m diameter, fitting these rocks to an exponential SFD model, and extrapolating along the model to predict the number of rocks smaller than 1.5 m that could be potentially hazardous to landing spacecraft (Golombek et al., 2008, Golombek, Huertas et al., 2012, Golombek, Kipp et al., 2017).

The average rock abundance of 4-5% (CFA) in the 1 km^2 area around the lander is consistent with thermal imaging estimates over larger pixel areas for the location of the lander. The InfaRed Thermal Mapper (IRTM) rock abundance in the 60 km pixel that contains the lander is 4% (Christensen, 1986). The nearest 7.5 km pixel Thermal Emission Spectrometer (TES) rock abundance estimate, about 10 km to the east, is 3.3% (7.5 km pixel) (Nowicki & Christensen, 2007) and the average TES rock abundance within 20 km of the lander is 3.7% (11 pixels).

5. Comparison of Rocks Measured on the Surface and from Orbit

Four rocks observed from the lander were also detected by the machine vision rock detection algorithm in the HiRISE image. The rocks mapped in the far field, Hanging rock (Figure 8), First rock (Figure 10), Gazebo rock (Figure 14), as well as the easternmost of the three Pinnacle rocks (Figure 7) were detected and counted using the standard machine vision algorithm (Golombek, Kipp et al. (2017). The rock detector employs a modified maximum entropy thresholding technique using a nonlinear image stretching routine that segments shadows cast by rocks from non-shadowed pixels and fits ellipses to shadows and cylinders to the rocks (Golombek et al., 2008). Deconvolution methods are used to sharpen the images, detect smaller

484 rock shadows, improve shadow segmentation, and differentiate and eliminate shadows not
485 produced by rocks (Golombek, Huertas et al., 2012).

486 Subsequent methods developed for the Mars 2020 Rover landing site selection
487 (Golombek, Otero et al., 2017) were used to systematically vary these parameters to detect a
488 larger sample of possible rocks that were used to define safe areas for landing. Different
489 combinations of three parameters and two sharpening techniques were iterated through a series
490 of runs, and combined to maximize the number of rocks that could be detected. Gamma, a
491 parameter which enhances shadow intensity, mean gradient threshold, a parameter which is used
492 to determine the edge of a shadow by comparing a shaded region to its background, shadow
493 aspect ratio, which is the ratio of a shadow length-to-width used to remove false positives like
494 eolian bedforms, and normalizing the image to remove common background signal were all
495 varied. After these parameter sweeps (a total of 168 runs), clusters of overlapping "duplicate"
496 detections were identified as groups of rocks within 7 cumulative pixels of each other using rock
497 position and diameter. Each cluster of "duplicate" detections was replaced with a rock that was
498 averaged from all of the detections. Hanging rock (Figure 8) was measured using this method.

499 These four rocks detected in the HiRISE image vary in distance from the lander from 19
500 m to 60 m and are shown on Figure 17 (three of them are shown on Figure 6). These rocks are
501 the largest rocks (diameter and height) observable from the lander (diameters 0.6-0.8 m, heights
502 0.3-0.5 m) and thus cast the largest shadows. Table 3 shows the diameters and heights derived
503 from the measurements in the surface panoramas (section 3.2) and in HiRISE. The difference in
504 diameter between the two methods is less than 0.03 m and the difference in heights between the
505 two methods is 0.09 m. The difference in diameter is less than 5%; the difference in height is less
506 than 23%. Previous tests of the performance of the rock detector on spacecraft of known size on

507 the surface of Mars shows the algorithm accurately determined spacecraft diameter and height to
508 within 1 – 2 pixels, which is about the limit of what could be expected (Golombek et al., 2008;
509 Golombek, Huertas et al, 2012). The differences in height and diameter of the four rocks
510 measured here is a small fraction of one pixel (27.5 cm/pixel in the NO MAP HiRISE image
511 ESP_036761_1845), which further documents the excellent signal to noise of the HiRISE
512 camera and the performance of the rock detection and measurement algorithm.
513
514 **6. Fragmentation**
515
516 The SFD of rocks measured from both the lander and orbit is consistent with estimates
517 made from fragmentation theory prior to landing (Golombek, Kipp et al., 2017). Fragmentation
518 theory (Charalambous, 2014) was used to model the particle size-frequency distribution of the
519 regolith (including the rock abundance) based on the rocks and craters measured in HiRISE
520 images (Golombek, Kipp et al., 2017) and negative binomials were fit to all rocks measured in
521 the landing ellipse. These fits are similar to the Phoenix and Spirit landing site rock size-
522 frequency distributions for diameters smaller than about 1 m (Golombek, Kipp et al., 2017,
523 Golombek, Kass et al., 2020). In this section, we explore this further using the near field, far
524 field and HiRISE rock counts.
525 Based on the probabilistic calculation of repeated fracture of a particle population, the
526 fragmentation theory developed by Charalambous (2014) allows an understanding of the time-
527 dependent processes that formed an observed rock population. Under repeated fracture events,
528 the ensemble of these fragmentation processes can be described by a negative binomial (NB)
529 function in which the rock-size distribution evolves over time at different rates according to the
530 maturity index, t and a probability of fracture, p. For the larger fragments on Mars (diameter >

~1 mm), the maturity index is dominantly determined by the number of meteorite impacts, which is constrained by age of the surface and the crater population. For smaller fragments ($d < \sim 1$ mm), the maturity index becomes increasingly determined by the activity of aeolian processes which contribute to the evolution of a grain distribution, most notably from the processes of saltation for sand-size particles, to creep for granule-size particles (Golombek et al., 2018 Golombek, Charalambous, 2020).

The NB fit for the InSight rock data was made to restricted portions of the three rock SFDs (Figure 18) to avoid the resolution roll off of the data where the image resolution resulted in fewer rocks measured (discussed earlier for each data set) and the SFDs shallow. Rocks with diameters below 1.2 m were omitted from the HiRISE data and those with diameters below 0.3 m diameter were omitted from the far field data (roughly where the far field SFD crosses the near field SFD). The three InSight rock distributions fit an estimated maturity index of $t = 3.3 \pm 0.3$ (Figure 18), and it falls within the error bounds of initial predictions made just from particle size measurements of InSight's workspace (Charalambous et al., 2019). Given the NB statistics, the observed rock population is therefore estimated to be the product of ~3 fragmentation events, or impacts, on average. The NB curve is consistent with the 5% exponential rock model curve matching the HiRISE rock counts for diameters greater than 1.6 m and fall between the 4% and 5% exponential model curves for smaller diameters.

NB fits for rock populations at other landing sites on Mars (Spirit, Phoenix, Viking Landers and Mars Pathfinder) share a common probability of fracture ($p = 0.75$, Golombek et al., 2017), indicative of the same underlying processes of fragmentation by impacts. Shown in Figure 18 are NB fits to the measured surface rock SFD at the Spirit and Phoenix landing sites (Golombek, Kipp et al. 2017). Both of these landing sites have the nearest rock SFDs to InSight

554 with close-to-parallel slopes to InSight's NB fit for total rock counts measured from both orbit
555 and surface cameras. The NB fit of the InSight rock abundance appears higher than the Phoenix
556 NB fit, but lower than the Spirit landing site. The close match to the Spirit landing site is
557 consistent with both predictions prior to landing (Golombek, Kipp et al., 2017) and the
558 appearance, as well as similar geological history of the two sites (impacted
559 Hesperian/Amazonian lava flows, Golombek, Kass et al., 2020). The similar multiplicity effect
560 of the NB statistics from multiple fragmentation events (here at t = 3.3) is suggestive of an
561 impact-comminuted rock population rich in sand-sized material (Golombek, Charalambous et al.,
562 2018, 2020), consistent with orbital thermal inertia measurements and the low rock abundance at
563 the landing site (Golombek, Kass et al., 2020). The observation that Amazonian impact cratering
564 of hard, relatively intact bedrock (basalt) can produce a meters-thick surface layer with low rock
565 abundance that is dominated by sand sized particles (at both the Spirit and InSight landing sites,
566 Golombek et al., 2006; Golombek, Warner et al., 2020), suggests that the global surface layer
567 composed of mostly fine grained materials on Mars (Christensen and Moore, 1992) is produced
568 mainly by impact and eolian processes (e.g., Golombek, Charalambous et al., 2018, 2020).
569
570 **7. Summary and Conclusions**
571
572 Rocks around the InSight lander in the near field, far field and in a HiRISE orbital image
573 were measured to produce rock size-frequency distributions (SFD), representing the first full
574 treatment of this type for this landing site. More than 2,000 rocks were counted in four areas
575 from an orthomosaic produced from 283 IDC images within 10 m of the lander. The SFD of the
576 four areas are similar to exponential model SFD curves, developed from the Viking Lander 1 and
577 2 rock SFDs, for rock abundances of <1% to ~5%. Altogether the SFD of the entire near field

has a cumulative fractional area (CFA) of ~3%, in between the ~2% rock abundance at the Phoenix and 5% rock abundance at the Spirit landing sites. The curved shape of the SFD of the InSight near field rocks is also similar to other landing sites on Mars as well as the exponential model curves.

Rocks within 40 m of the lander that could be identified in both the surface, controlled panorama and in a sharpened NOMAP HiRISE image were also measured by determining their distance in HiRISE and their size from the IDC pixel scale. Eighty-two far field rocks 0.1-0.6 m diameter were measured. The illuminated and shadowed portions (bright-dark pixel pairs) of rocks could be identified even if the rocks are smaller than the HiRISE pixels, likely a result of the excellent signal to noise of the HiRISE camera. The SFD of the CFA versus diameter of rocks in the far field follow the ~3% model curve for diameters of 0.4 m to 0.9 m, which is the same model curve for all near field rocks with diameters of 0.03-0.4 m.

Rocks measured with the machine vision rock detection algorithm used to determine rock abundance during landing site selection and verified by a human within a 1 km^2 area centered on the lander are parallel to exponential model curves for 4%-5% rock abundance for rocks 1.2-2.0 m diameter. This CFA SFD is similar to the rock abundance of rockier areas in the near field to the north and west of the lander and is within 1%-2% of the average near and far field rock abundances. As a result, the rock abundances observed from orbit fall on similar exponential model rock abundance curves as those viewed from the surface, similar to the Viking Lander 2, Mars Pathfinder, Phoenix and Spirit landing sites. This further strengthens the use of HiRISE images to measure rocks >1.5 m in diameter, fitting these rocks to an exponential SFD model, and extrapolating along the model to predict the number of rocks smaller than 1.5 m that could be potentially hazardous to landing spacecraft. Rock abundance measurements at the InSight

601 landing site are also consistent with thermal imaging estimates over larger pixel areas for the
602 location of the lander. Four rocks detected and measured in the machine vision algorithm of the
603 HiRISE image that could be measured from the lander have diameters (0.6-0.8 m) that agree
604 within 5% and heights (0.3-0.6 m) that agree to within 23%, all within a fraction (<10%) of a
605 HiRISE pixel.

606 The SFD of rocks measured from both the lander and orbit is consistent with estimates
607 made from fragmentation theory used to model the particle size-frequency distribution based on
608 the rocks and craters measured in HiRISE images. A negative binomial (NB) function based on
609 the number of fragmentation events and the probability of failure, was fit to near field, far field
610 and HiRISE measured SFD of rocks (excluding portions of the SFDs with resolution roll off,
611 from the camera resolution). The NB curve is similar to the 4%-5% SFD exponential model
612 curves and share a common number of fragmentation events and probability of failure as the
613 Spirit and Phoenix SFD of rocks. This commonality in fragmentation to produce landing sites
614 dominated by fine particles with low rock abundance suggests that the global, meters-thick
615 surface layer on Mars, made up mostly of find-grained materials, can be produced mainly by
616 impact cratering during the Amazonian.

617

618

619

620 **Data Availability Statement**

621

622 All InSight image data discussed in this paper are in the Planetary Data System
623 Geosciences node (https:// pds-geosciences.wustl.edu/missions/insight/index.htm). All other
624 Mars imaging data are in the Cartography and Imaging Node (https://pds-imaging.jpl.nasa.gov/).

The HiRISE orthoimage and DEM in which the lander is located are available at https://www.uahirise.org/dtm/dtm.php?ID=ESP_037262_1845 (Fergason et al., 2017), and other HiRISE images acquired are available via the HiRISE website at https://hirise.lpl.arizona.edu/. The HiRISE orthoimage and DEM produced by Fergason et al. (2017) in which the lander is located are also available in Golombek (2020). The morning, midday (afternoon) and evening InSight IDC panoramas used to create Figures 7–14 are also available in Golombek (2020). The IDC orthomosaic, DEM and shape files of rocks measured in the near field (Figure 1) are available in Golombek (2021).

Acknowledgements

A portion of this work was supported by the InSight Project at the Jet Propulsion Laboratory, California Institute of Technology, under a contract with the National Aeronautics and Space Administration. We thank Alfred McEwen for information and discussion about the HiRISE camera. This paper is InSight Contribution Number ICN-204.

References

Abarca, H., Deen, R., Hollins, G., Zamani, P., Maki, J., Tinio, A., et al. (2019). Image and data processing for InSight lander operations and science. Space Science Reviews, 215(2), 22. https://doi.org/10.1007/s11214-019-0587-9

Arvidson, R., D. Adams, G. Bonfiglio, P. Christensen, S. Cull, M. Golombek et al. (2008). Mars Exploration Program 2007 Phoenix landing site selection and characteristics. Journal of Geophysical Research, 113, E00A03, doi:10.1029/2007JE003021.

Binder, A. B., R. E. Arvidson, E. A. Guinness, et al. (1977). The geology of the Viking Lander 1 site. Journal of Geophysical Research 82, 4439–51.

Brown, W. K., and K. H. Wohletz (1995). Derivation of the Weibull distribution based on physical principles and its connection to the Rosin-Rammler and lognormal distributions. Journal of Applied Physics 78, 2758– 2763.

Charalambous, C. (2014). On the evolution of particle fragmentation with applications to planetary surfaces. PhD Thesis, Imperial College London.

Charalambous, C., Golombek, M., Pike, T., Warner, N. H., Weitz, C., Ansan, V., et al. (2019). Rock distributions at the InSight landing site and implications based on fragmentation theory. 50th Lunar and Planetary Science, Abstract #2812, Lunar and Planetary Institute, Houston.

Charalambous, C., McClean, J. B., Baker, M., Pike, W. T., Golombek, M., et al. (2020). Aeolian Vortex-dominated aeolian activity at InSight's landing site, Part 1: Multi-instrument observations, analysis and implications. Journal of Geophysical Research, Planets, 126, e2020JE006757, doi: 10.1029/2020JE006757

Christensen, P. R. (1986). The spatial distribution of rocks on Mars. Icarus, 68(2), 217–238. https://doi.org/10.1016/0019-1035(86)90020-5

Christensen, P. R., & Moore, H. J. (1992). The Martian surface layer. In H. H. Kieffer, B. M. Jakosky, C. W. Snyder, & M. S. Matthews (Eds.), Mars (pp. 686–727). Tucson: University of Arizona Press.

671 Craddock, R.A., and M. P. Golombek (2016). Characteristics of terrestrial basaltic rock
672 populations: Implications for Mars lander and rover science and safety. Icarus 274, 50–72
673 https://doi.org/10.1016/j.icarus.2016.02.042
674 Fergason, R., Kirk, R. L., Cushing, G., Galuzska, D. M., Golombek, M. P., Hare, T. M., et al.
675 (2017). Analysis of local slopes at the InSight landing site on Mars. Space Science
676 Reviews, 211(1-4), 109–133. https://doi.org/10.1007/s11214-016-0292-x
677 Garvin, J. B., P. J. Mouginis-Mark and J. W. Head (1981). Characterization of rock populations
678 on planetary surfaces: Techniques and a preliminary analysis of Mars and Venus. Moon
679 and Planets 24, 355 – 387.
680 Gilvarry, J. J. (1961). Fracture of brittle solids I. Distribution function for fragment size in single
681 fracture (theoretical). Journal of Applied Physics 32, 391– 399.
682 http://dx.doi.org/10.1063/1.1736016
683 Gilvarry, J. J. and B. H. Bergstrom (1961). Fracture of brittle solids II. Distribution function for
684 fragment size in single fracture (experimental). Journal of Applied Physics 32, 400– 410.
685 http://dx.doi.org/10.1063/1.1736017
686 Golombek, M. (2020). Data for “Assessment of InSight landing site predictions” [data set].
687 CaltechDATA. https://doi.org/10.22002/D1.1422
688 Golombek, M. (2021). Data for Golombek et al. paper “InSight Rock size-frequency
689 distributions on Mars” [data set] submitted to the journal Earth and Space Science.
690 https://doi.org/10.48577/jpl.CMZSTZ
691 Golombek, M., and D. Rapp (1997). Size-frequency distributions of rocks on Mars and Earth
692 analog sites: Implications for future landed missions. Journal of Geophysical Research
693 102, 4117-4129. http://dx.doi.org/10.1029/96JE03319

694 Golombek, M. P., Cook, R. A., Moore, H. J., & Parker, T. J. (1997). Selection of the Mars
695 Pathfinder landing site. Journal of Geophysical Research, 102(E2), 3967–3988.
696 https://doi.org/10.1029/96JE03318
697 Golombek, M. P., Haldemann, A. F. C., Forsberg-Taylor, N. K., DiMaggio, E. N., Schroeder, R.
698 D., Jakosky, B. M., et al. (2003). Rock size-frequency distributions on Mars and
699 implications for Mars Exploration Rover landing safety and operations. Journal of
700 Geophysical Research, 108(E12), 8086. https://doi.org/10.1029/2002JE002035
701 Golombek, M. P., Grant, J. A., Parker, T. J., Kass, D. M., Crisp, J. A., Squyres, S. W., et al.
702 (2003). Selection of the Mars Exploration Rover landing sites. Journal of Geophysical
703 Research, 108(E12), 8072. https://doi.org/10.1029/2003JE002074
704 Golombek, M. P., Crumpler, L. S., Grant, J. A., Greeley, R., Cabrol, N. A., Parker, T. J., et al.
705 (2006). Geology of the Gusev cratered plains from the Spirit rover traverse. Journal of
706 Geophysical Research, 111, E02S07. https://doi.org/10.1029/2005JE002503
707 Golombek, M. P., Huertas, A., Marlow, J., McGrane, B., Klein, C., Martinez, M., et al. (2008).
708 Size-frequency distributions of rocks on the northern plains of Mars with special
709 reference to Phoenix landing surfaces. Journal of Geophysical Research, 113, E00A09.
710 https://doi. org/10.1029/2007JE003065
711 Golombek, M., Huertas, A., Kipp, D., & Calef, F. (2012). Detection and characterization of
712 rocks and rock size-frequency distributions at the final four Mars Science Laboratory
713 landing sites. International Journal of Mars Science and Exploration 7, 1–22.
714 https://doi.org/10.1555/mars.2012.0001

715 Golombek, M., Grant, J., Kipp, D., Vasavada, A., Kirk, R., Fergason, R., et al. (2012). Selection
716 of the Mars Science Laboratory landing site. Space Science Reviews, 170(1-4), 641–737.
717 https://doi.org/10.1007/s11214-012-9916-y
718 Golombek, M. P., Otero, R. E., Heverly, M. C., Ono, M., Williford, K. H., Rothrock, B.,
719 Milkovich, S., Almeida, E., Calef, F., Williams, N., Ashley, J., and Chen, A. (2017).
720 Characterization of Mars Rover 2020 prospective landing sites leading up to the second
721 downselection. 48th Lunar and Planetary Science, Abstract #2333, Lunar and Planetary
722 Institute, Houston.
723 Golombek, M., Kipp, D., Warner, N., Daubar, I. J., Fergason, R., et al. (2017). Selection of the
724 InSight landing site. Space Science Reviews, 211(1-4), 5–95.
725 https://doi.org/10.1007/s11214-016-0321-9
726 Golombek, M. P., Charalambous, C., Pike, W. T., and Sullivan, R. (2018). The origin of sand on
727 Mars. 49th Lunar and Planetary Science, Abstract #2319, Lunar and Planetary Institute,
728 Houston.
729 Golombek, M., Kass, D., Williams, N., Warner, N., Daubar, I., Piqueux, S., Charalambous, C.,
730 and Pike, W. T. (2020). Assessment of InSight landing site predictions: Journal of
731 Geophysical Research, Planets, 125, e2020JE006502. https://dx.doi.org/
732 10.1029/2020JE006502.
733 Golombek, M., Charalambous, C., Pike, W. T., and Sullivan, R. (2020). The origin of sand and
734 dust on Mars: Evidence from the InSight landing site. 51st Lunar and Planetary Science,
735 Abstract #2744, Lunar and Planetary Institute, Houston.

736 Golombek, M., Warner, N. H., Grant, J. A., Hauber, E., Ansan, V., Weitz, C. M., et al. (2020).
737 Geology of the InSight landing site on Mars. Nature Communications, 11, 1014,
738 https://doi.org/10.1038/s41467-020-14679-1
739 Golombek, M., Williams, N., Warner, N. H., Parker, T., Williams, M. G., Daubar, I., et al.
740 (2020). Location and setting of the Mars InSight lander, instruments, and landing site.
741 Earth and Space Science, 7, e2020EA001248. https://doi.org/10.1029/2020EA001248
742 Grant, J. A., Wilson, S. A., Ruff, S. W., Golombek, M. P., & Koestler, D. L. (2006). Distribution
743 of rocks on the Gusev Plains and on Husband Hill, Mars. Geophysical Research Letters,
744 33, L16202. https://doi.org/10.1029/2006GL026964
745 Grant, J. A., Warner, N. H., Weitz, C. M., Golombek, M. P., Wilson, S. A., Baker, M., et al.
746 (2020). Degradation of Homestead hollow at the InSight landing site based on the
747 distribution and properties of local deposits. Journal of Geophysical Research: Planets,
748 125, e2019JE006350. https://doi.org/ 10.1029/2019JE006350
749 Hébrard, E., C. Listowski, P. Coll, B. Marticorena, G. Bergametti, A. Määttänen, F. Montmessin,
750 and F. Forget (2012) An aerodynamic roughness length map derived from extended
751 Martian rock abundance data. Journal of Geophysical Research 117, E04008
752 http://dx.doi.org/10.1029/2011JE003942
753 Heet, T. L., R. E. Arvidson, S. C. Cull, M. T. Mellon and K. D. Seelos (2009). Geomorphic and
754 geologic settings of the Phoenix Lander mission landing site. Journal of Geophysical
755 Research 114, E00E04 http://dx.doi.org/10.1029/2009JE003416
756 Maki, J. N., Golombek, M., Deen, R., Abarca, H., Sorice, C., Goodsall, T., et al. (2018). The
757 color cameras on the InSight lander. Space Science Reviews, 214(105).
758 https://doi.org/10.1007/s11214-018-0536-z

759 Moore, H. J. and J. M. Keller (1990). Surface-material maps of Viking landing sites on Mars.
760 Reports of Planetary Geology and Geophysics Program – 1989, NASA Tech. Memo.,
761 4210, 533–535.
762 Moore, H. J. and J. M. Keller (1991). Surface-material maps of Viking landing sites on Mars.
763 Reports of Planetary Geology and Geophysics Program – 1990, NASA Tech. Memo.,
764 4300, 160–162.
765 Moore, H. J., C. R. Spitzer, K. Z. Bradford, P. M. Cates, R. E. Hutton, and R. W. Shorthill
766 (1979). Sample fields of the Viking landers, Journal of Geophysical Research 84, 8365-
767 8377.
768 Nowicki, S. A., and Christensen, P. R. (2007). Rock abundance on Mars from the Thermal
769 Emission Spectrometer. Journal of Geophysical Research, 112, E05007.
770 https://doi.org/10.1029/2006JE002798
771 Rosin, P. and E. Rammler (1933), The laws governing the fineness of powdered coal, Journal
772 Inst. Fuel 7, 29–36.
773 Russell, P. S., J. A. Grant, K. K. Williams, L. M. Carter, W. Brent Garry, and I. J. Daubar
774 (2013). Ground penetrating radar geologic field studies of the ejecta of Barringer
775 Meteorite Crater, Arizona, as a planetary analog. Journal of Geophysical Research 118,
776 1915–1933, doi:10.1002/jgre.20145
777 Turcotte, D. L. (1997). Fractals and Chaos in Geology and Geophysics, 2nd ed. (Cambridge U.
778 Press, Cambridge).
779 Ward, J. G., R. E. Arvidson, and M. Golombek (2005). The size-frequency and areal distribution
780 of rock clasts at the Spirit landing site, Gusev crater, Mars. Geophysical Research Letters
781 32, L11203 http://dx.doi.org/10.1029/2005GL022705

782 Warner, N. H., Grant, J. A., Wilson, S., Golombek, M. P., DeMott, A., Charalambous, C., et al.
783 (2020). An impact crater origin for the InSight landing site at Homestead hollow:
784 Implications for near surface stratigraphy, surface processes, and erosion rates. Journal of
785 Geophysical Research: Planets 125, e2019JE006333.
786 https://doi.org/10.1029/2019JE006333
787 Wohletz, K. H., M. F. Sheridan and W. K. Brown (1989). Particle size distributions and the
788 sequential fragmentation/transport theory applied to volcanic ash. Journal of Geophysical
789 Research 94, 15,703– 15,721. http://dx.doi.org/10.1029/JB094iB11p15703
790 Yingst, R. A., A. F. C. Haldemann, K. L. Biedermann and A. M. Monhead (2007). Quantitative
791 morphology of rocks at the Mars Pathfinder landing site. Journal of Geophysical
792 Research 112, E06002 http://dx.doi.org/10.1029/2005JE002582
793 Yingst, R. A., L. Crumpler, W. H. Farrand, R. Li and P. de Souza (2010). Constraints on the
794 geologic history of 'Home Plate' materials provided by clast morphology and texture.
795 Journal of Geophysical Research 115, E00F13 http://dx.doi.org/10.1029/2010JE003668
796 Yingst, R. A., L. C. Kah, M. Palucis, R. M. E. Williams, J. Garvin, J. C. Bridges, et al. (2013).
797 Characteristics of pebble- and cobble-sized clasts along the Curiosity rover traverse from
798 Bradbury Landing to Rocknest. Journal of Geophysical Research Planets, 118, 2361–
799 2380, doi:10.1002/2013JE004435.
800 Yingst, R.A., K. Cropper, S. Gupta, L.C. Kah, R.M.E. Williams, J. Blank, F. Calef III, V.E.
801 Hamilton, et al. (2016). Characteristics of pebble and cobble-sized clasts along the
802 Curiosity rover traverse from sol 100 to 750: Terrain types, potential sources, and
803 transport mechanisms. Icarus 280 (2016) 72–92,
804 http://dx.doi.org/10.1016/j.icarus.2016.03.001

Tables and Figures v. 3

Table 1. Area and number of rocks and those >3 cm diameter counted in four near-field regions around InSight.

Region	Area (m^2)	All Rocks	Rocks > 3 cm
North	75.29	533	328
East	30.69	90	45
South	60.13	1160	266
West	41.20	234	215
All	207.31	2017	854

Table 2. Azimuth, measured clockwise from north in HiRISE, distance measured in HiRISE, apparent diameter and height of rocks in the far field. Large, named rocks from (Golombek, Williams et al., 2020).

Rock Name and Abbreviation	Azimuth in HiRISE (deg)	Distance in HiRISE (m)	Apparent Diameter (m)	Height (m)
Piano Rock	0	8.5	0.18	0.14
Bench Rock	0	8.5	0.21	0.08
Pedal Rock	1	8.5	0.21	0.14

31	22	14.7	0.23	0.16
32	24	21.4	0.2	0.19
30	25	16.7	0.35	0.24
33	28	21.1	0.24	0.15
Slippery Rock, SR	40	13.8	0.55	0.32
34	41	20.2	0.24	0.14
35	45	22.6	0.32	0.26
WoT Rock	47	44.8	0.44	0.3
135	50	29.7	0.38	0.22
Hanging Rock, HR	53	20.7	0.59	0.52
136	57	29.2	0.13	0.13
137	63	28.4	0.26	0.17
36	64	25.8	0.52	0.32
37	69	26.4	0.36	0.29
38	69	27.7	0.53	0.29
39	83	26	0.4	0.3
40	88	23.3	0.23	0.17
Table Rock, T	106	17.6	0.4	0.22
School House Rock, SH	107	19.6	0.53	0.19
41	112	27.7	0.39	0.26
42	119	25.1	0.34	0.11
43	125	25.9	0.35	0.19
Cone Rock, CN	128	32.8	0.58	0.34
143	130	42	0.47	0.18
44	136	21.9	0.34	0.27
144	136	28.6	0.3	0.21
Flat Top Rock, FT	138	14.8	0.52	0.1
145	140	31.8	0.23	0.18
146	146	23.7	0.17	0.15
45	150	22	0.41	0.32
46	155	27	0.43	0.23
147	155	34.5	0.32	0.21
148	157	35.7	0.22	0.18
First Rock, FR	160	19.4	0.78	0.41
47	162	22.7	0.59	0.28
149	166	33.7	0.25	0.12
48	167	22	0.35	0.24
150	167	32.7	0.32	0.16
49	175	21.3	0.35	0.25

50	206	21.4	0.27	0.12
51	209	23.7	0.27	0.14
Mailbox 1 Rock, MB-1	212	22.2	0.41	0.27
Mailbox 2 Rock, MB-2	212	22.2	0.34	0.18
52	217	22.7	0.49	0.11
53	219	20.7	0.23	0.17
54	223	20	0.23	0.17
55	232	20.8	0.24	0.21
Calzone Rock	236	8.1	0.4	0.13
56	237	21.7	0.25	0.14
Meatball Rock	240	5.1	0.21	0.13
157	240	28.5	0.3	0.13
57-1	242	26.3	0.21	0.11
57-2	242	26.3	0.24	0.11
58	245	23.8	0.21	0.11
Pyramid 1 Rock	248	9.6	0.12	0.07
Pyramid 2 Rock	248	9.6	0.26	0.22
Pyramid 3 Rock	248	9.6	0.17	0.11
59	249	19.6	0.28	0.19
Sphinx Rock	250	9.6	0.29	0.21
60	255	20.7	0.19	0.09
61	257	25.3	0.25	0.07
63	272	27.2	0.23	0.15
62	274	9.2	0.17	0.06
Porcupine Rock	279	10.7	0.21	0.09
Biscuit Rock	283	17.9	0.3	0.17
64	290	23.8	0.16	0.12
65	290	23.8	0.22	0.11
164	293	26.1	0.3	0.14
Churro Rock, CHR	299	22.8	0.47	0.25
66	315	19.5	0.18	0.15
Porpoise Rock	331	24.4	0.46	0.14
69	340	21.4	0.17	0.17
Hedgehog Rock, HH	347	21.5	0.32	0.19
Gazebo Rock, GZB	347	35.4	0.59	0.31
Slug Rock, SG	354	21.6	0.61	0.28
68	355	10.5	0.15	0.11
67	356	17.8	0.29	0.17
Snail Rock	356	13.5	0.33	0.21

Table 3. Comparison of rock diameter and height of rocks detected by the machine vision algorithm in the HiRISE image and in IDC images of the far field from the lander.

Rock Name	HiRISE Diameter (m)	Far Field Diameter (m)	Diameter Difference (m)	HiRISE Height (m)	Far Field Height (m)	Height Difference (m)
Pinnacle E Rock*	0.58	0.60	0.02	0.30	0.28	0.02
Hanging Rock	0.58	0.59	0.01	0.41	0.52	0.09
First Rock	0.81	0.78	0.03	0.32	0.41	0.09
Gazebo Rock	0.59	0.59	0.004	0.32	0.31	0.01

*At a distance of 60 m and an azimuth of 28°.

839

840

841

842

843

844

845

846

847

848 InSight Rock Figures

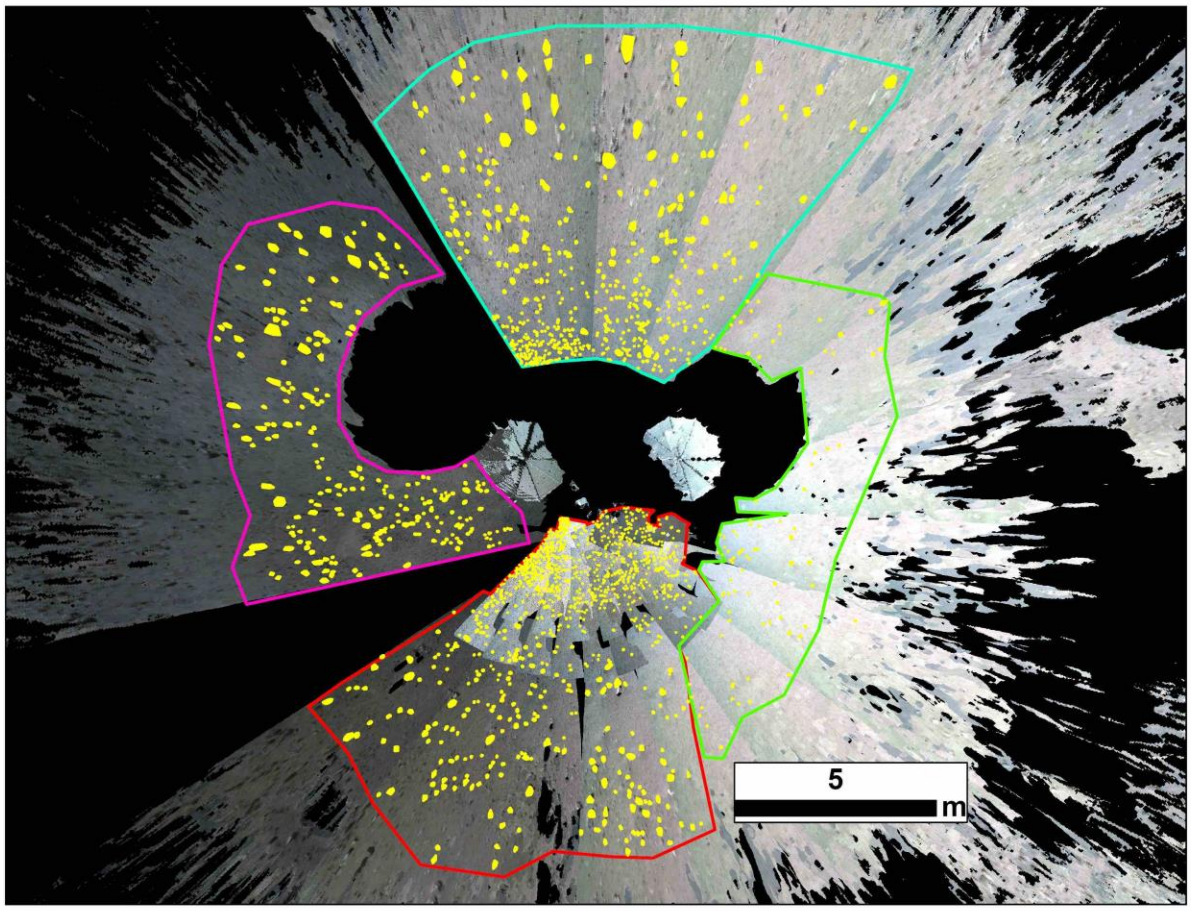

Figure 1. Orthomosiac (north up), produced from panorama digital elevation model, of the four areas around the InSight lander in which rocks (yellow) were counted (North, dark green; South, red; East, light green; West, pink). The N area is largest and the E area is the smallest. The S area has the largest number of rocks. Note the gaps separating the west area from the rest of the orthomosaic.

849
850
851
852
853
854
855
856

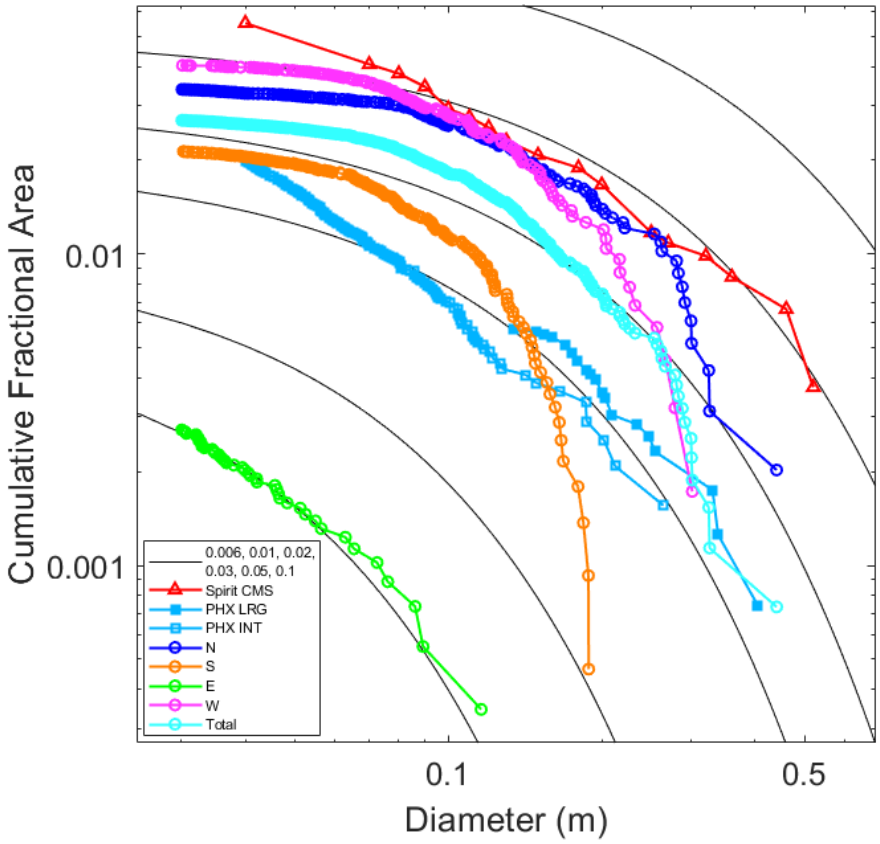

Figure 2. The cumulative fractional area of rocks larger than any given diameter versus diameter for the rocks measured in the four near field areas: north (N), south (S), east (E), and west (W) shown in Figure 1, and all near field rocks along with exponential model curves (Golombek and Rapp, 1997) for different total CFA or k of 0.6%, 1%, 2%, 3%, 5% and 10%. Also shown are the rocks measured at the Phoenix (Heet et al., 2009; Golombek, Huertas et al., 2012) and Spirit landing sites (Golombek et al., 2006) as plotted in Golombek, Huertas et al. (2012).

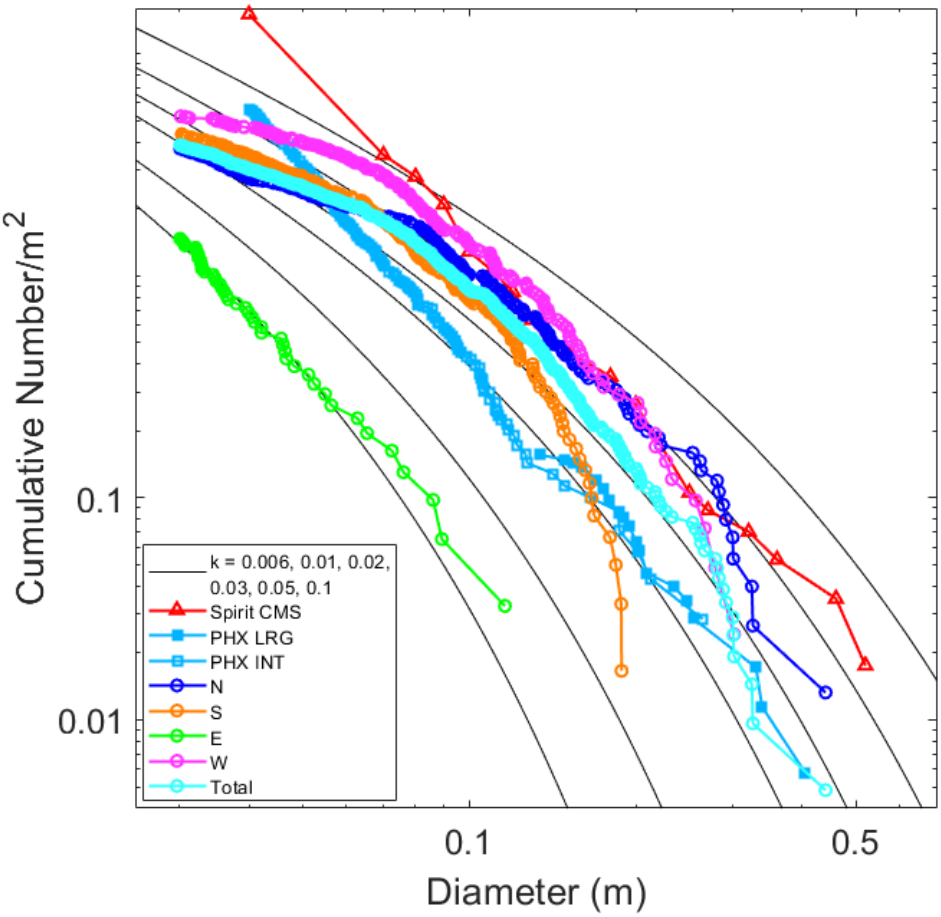

Figure 3. The cumulative number of rocks per m^2 larger than any given diameter versus diameter for the rocks measured in the four near field areas: north (N), south (S), east (E), and west (W) shown in Figure 1 and all near field rocks along with exponential model curves for different total CFA or k shown (Golombek and Rapp, 1997; Golombek, Haldemann et al., 2003). Also shown are the rocks measured at the Phoenix (Heet et al., 2009; Golombek, Huertas et al., 2012) and Spirit landing sites (Golombek et al., 2006) as plotted in Golombek, Huertas et al. (2012).

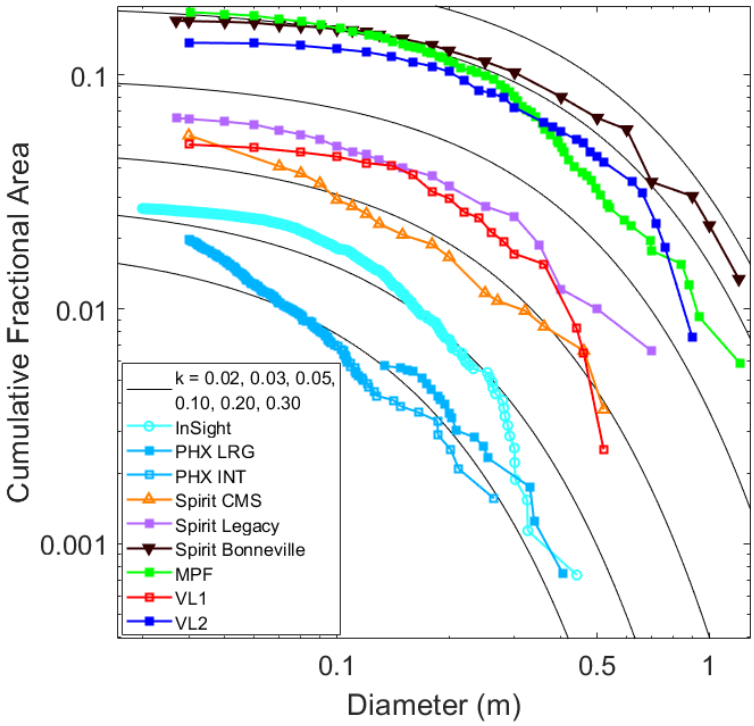

Figure 4. The cumulative fractional area of rocks larger than any given diameter versus diameter for the rocks measured from the surface of Mars along with exponential model curves for different total CFA or k of 2%, 3%, 5%, 10%, 20%, and 30% (Golombek and Rapp, 1997). Sources of rocks measured at Viking Lander 1, Viking Lander 2 (Moore and Keller, 1990, 1991), Mars Pathfinder (Golombek, Haldemann et al., 2003), Spirit (Golombek et al., 2006), Phoenix (Heet et al., 2009; Golombek, Huertas et al., 2012) (all replotted in Golombek, Huertas et al., 2012) and InSight (this paper).

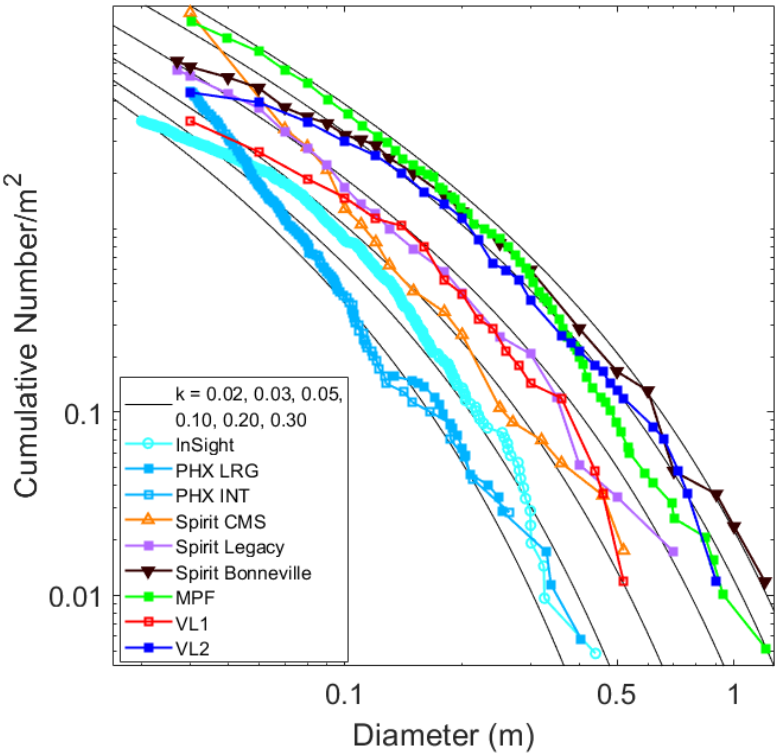

Figure 5. The cumulative number area of rocks per m^2 larger than any given diameter versus diameter for rocks measured from the surface of Mars along with exponential model curves for different total CFA or k shown (Golombek and Rapp, 1997; Golombek, Haldemann et al., 2003). Sources of rocks measured at Viking Lander 1, Viking Lander 2 (Moore and Keller, 1990, 1991), Mars Pathfinder (Golombek, Haldemann et al., 2003), Spirit (Golombek et al., 2006), Phoenix (Heet et al., 2009; Golombek, Huertas et al., 2012) (all replotted in Golombek, Huertas et al., 2012) and InSight (this paper).

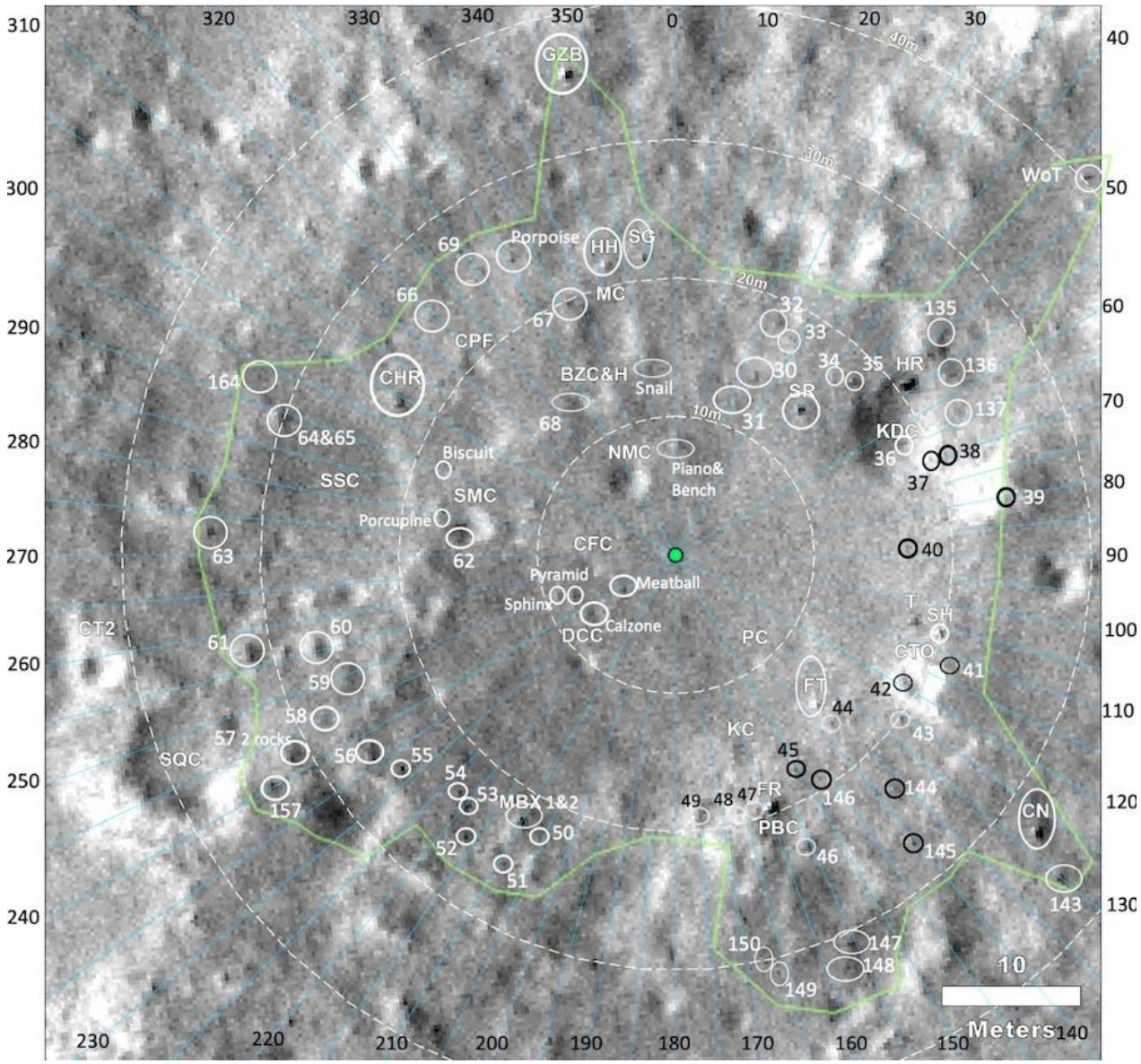

Figure 6. HiRISE image of the area around the InSight lander (green dot) with craters and rocks that can be identified in both the panoramas as well as this orbital image. Rocks are circled and either numbered or named (abbreviations) in Table 2, which includes the azimuth, distance, diameter and height. These rocks are identified in the surface panoramas in the subsequent figures. Green line encloses area used to determine the SFDs. Outside black numbers are azimuths in degrees (blue lines every 5°) clockwise from north. Dashed white circles are distances from the lander in 10 m increments. Craters clockwise from due north (up on the image), abbreviations are: KDC is Knee Deep crater, CTO is Corintito crater, PC is Puddle crater, PBC is Peekaboo crater, KC is Kettle crater, DCC is Deep Cut crater, SQC is Squash crater, CT2 is Corintitwo crater, CFC is Coffee crater, SMC is Smudge crater, SSC is Sunset crater, CPF is Campfire crater, BZC&H is Blast Zone crater and hollow, NMC is Near Miss crater, and MC is Mole crater. Named rocks and craters from Golombek, Williams et al. (2020). HiRISE image number ESP_036761_1845, is not map projected at 27.5 cm/pixel, with the Sun 54° from vertical from the northwest, azimuth 293° measured clockwise from north), but has

been georeferenced into a map view and contrast enhanced to emphasize illuminated rock bright sides to the northwest and shadows in the solar azimuth to the southeast.

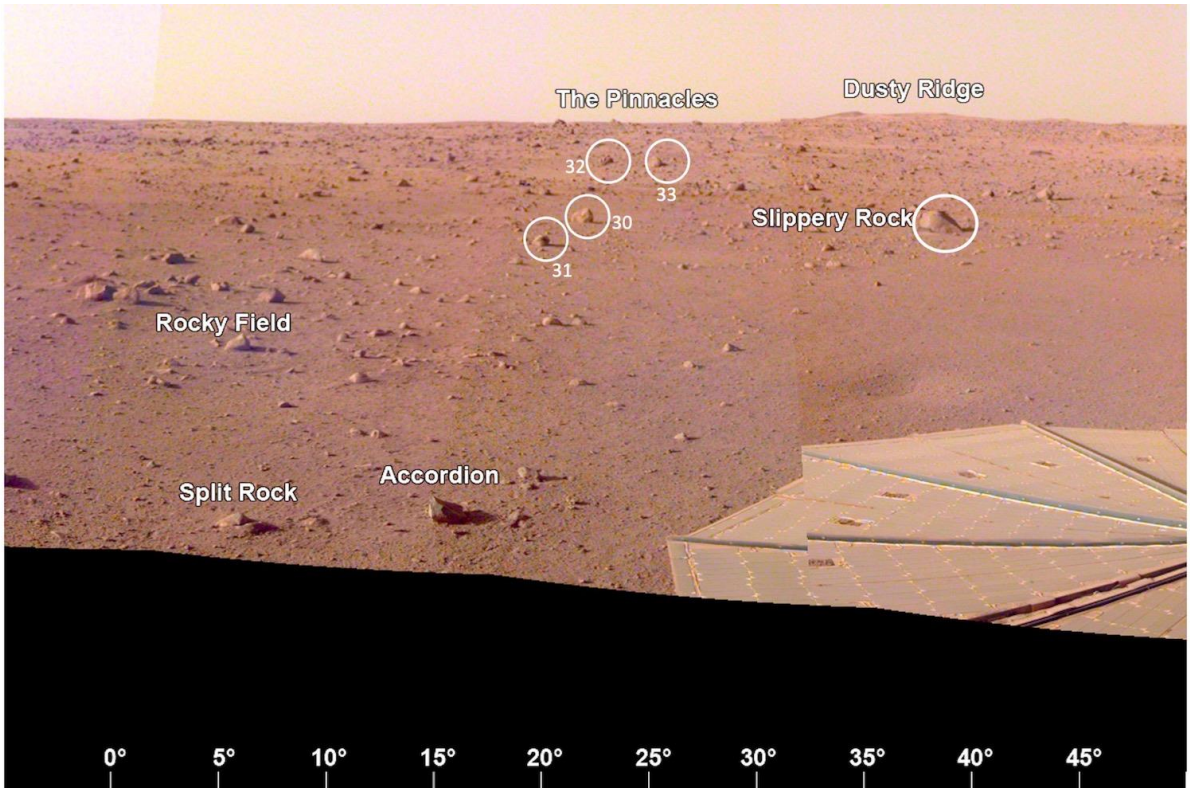

Figure 7. The view from the lander looking to the north-northeast (0° to 50°) showing measured rocks (circled), part of the solar panel, Rocky field, the smooth terrain to the east (right) and rockier terrain outside *Homestead hollow*. On the horizon are The Pinnacles rocks (three) and Dusty ridge, an eolian bedform about 50 m away on the rim of a 100 m diameter degraded impact crater. A portion of the evening panorama that has been stretched and is not true color.

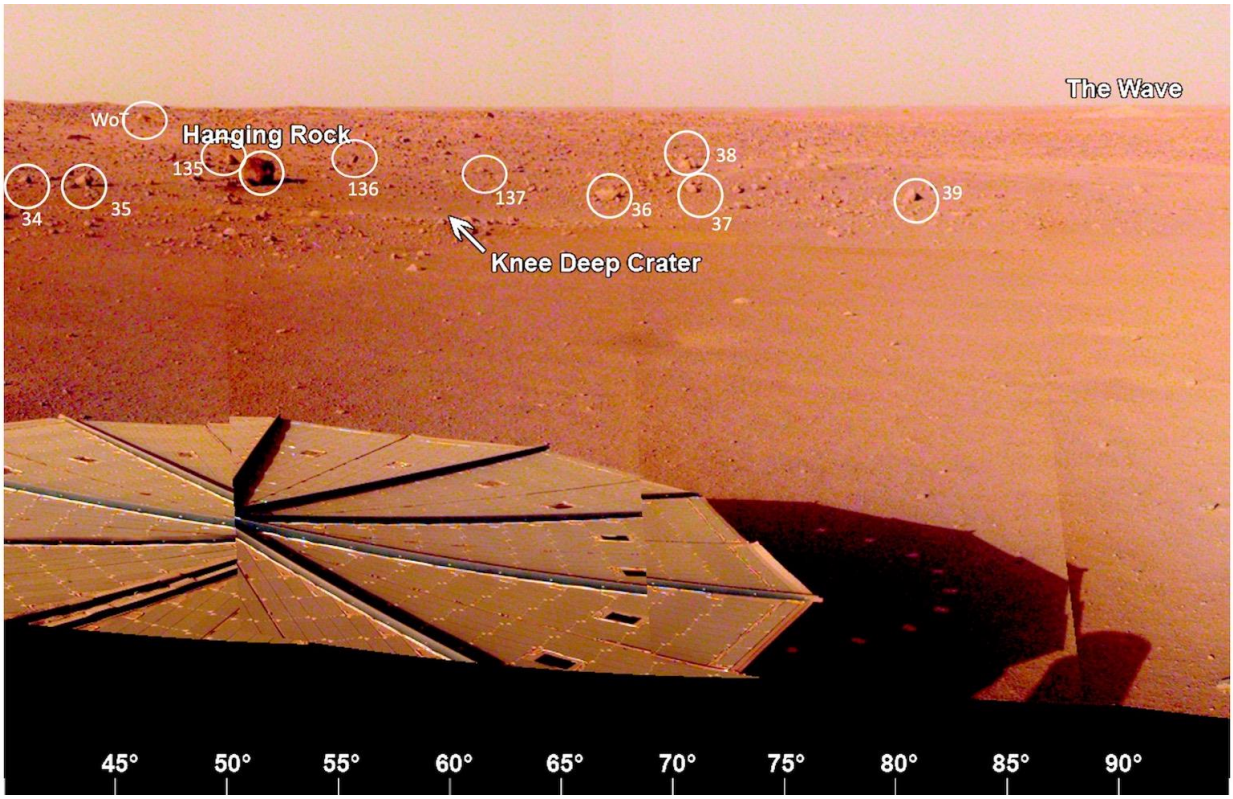

Figure 8. The view from the lander looking to the east-northeast (40° to 95°) showing measured rocks (circled), solar panel, the smooth terrain of *Homestead hollow* out to around 15 m. The eolian bedform, The Wave is on the horizon around 400 m away to the east. A portion of the evening panorama that has been stretched and is not true color.

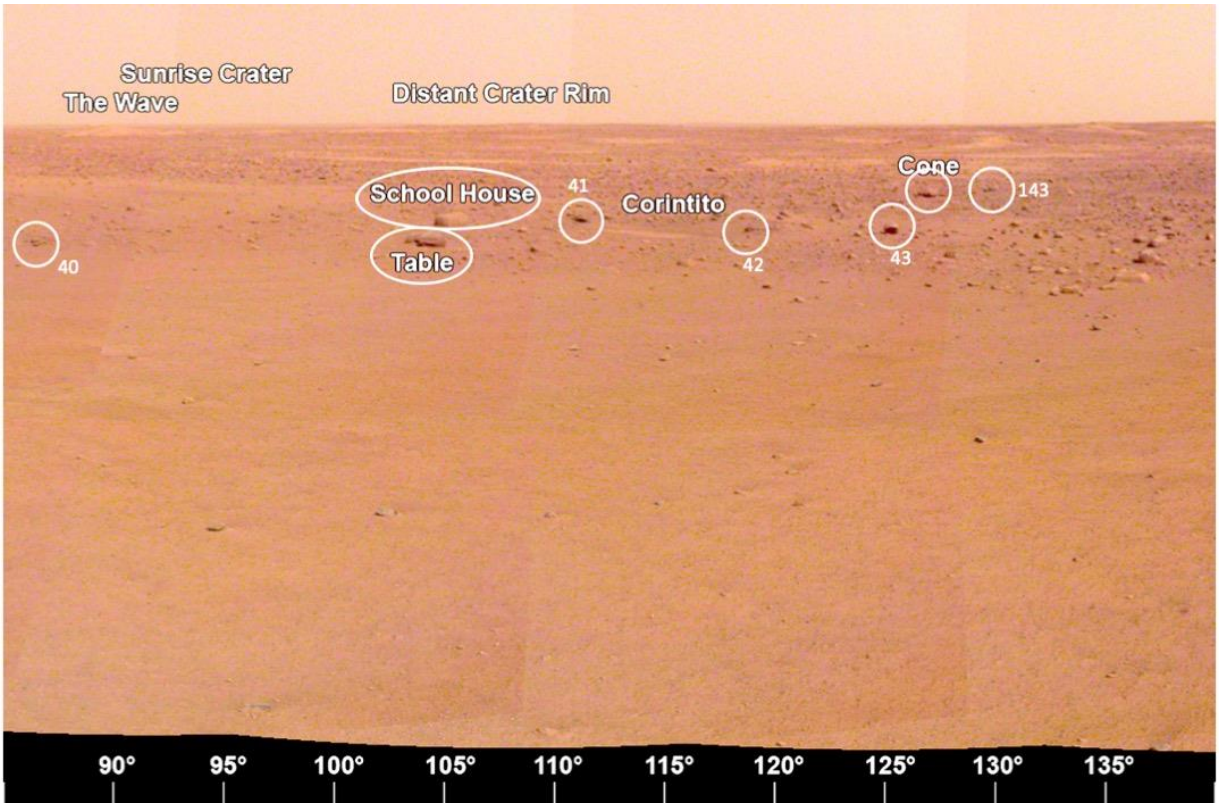

Figure 9. The view from the lander looking to the east-southeast (90° to 140°) showing the measured rocks (circled) and smooth terrain of *Homestead hollow* out to around 15 m. Note Corintito crater (a Corinto secondary crater in view, Golombek, Kipp et al., 2017, Golombek, Warner et al., 2020) is about 20 m away. In the distance, The Wave, a bright eolian bedform and the Sunrise crater rim, are on the horizon around 400 m away. The rim of a larger (460 m diameter), relatively fresh Distant crater can be seen on the east-southeast horizon ~2.4 km away. A portion of the afternoon panorama that has been stretched and is not true color.

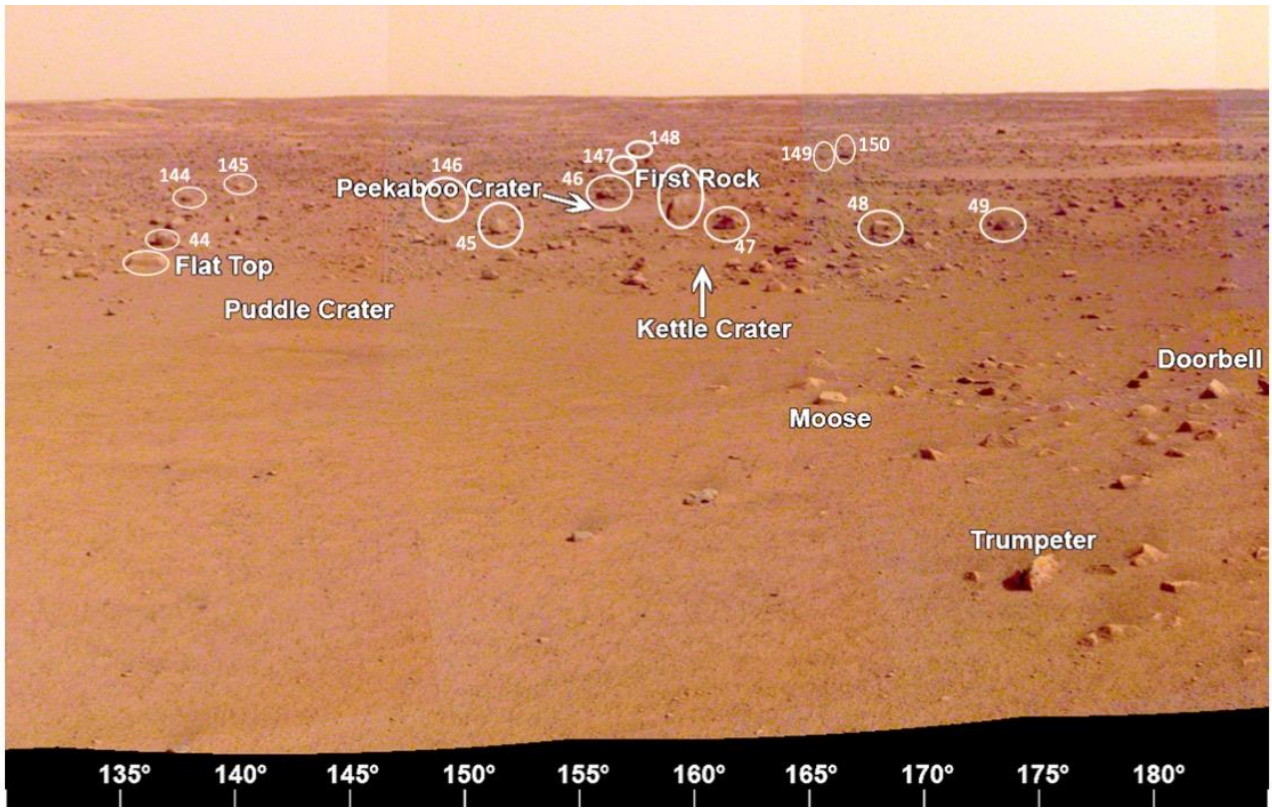

Figure 10. The view from the lander looking to the south-southeast (130° to 185°) showing measured rocks (circled), the smooth terrain of *Homestead hollow* with the rockier terrain beyond. A portion of the afternoon panorama that has been stretched and is not true color.

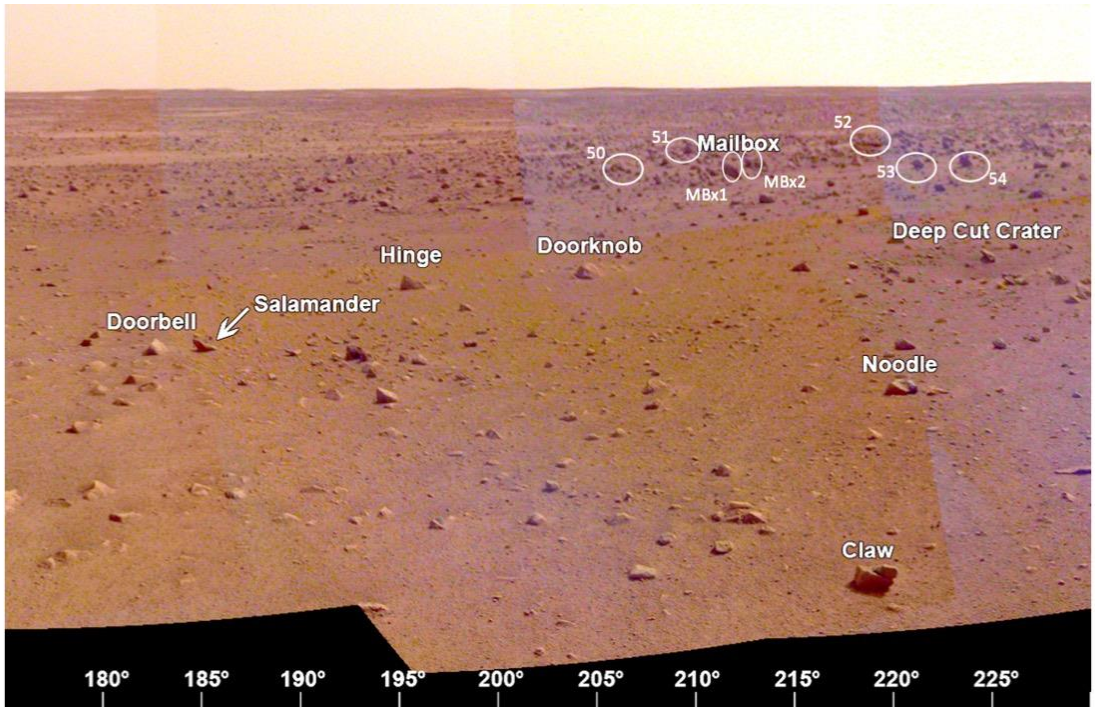

Figure 11. The view from the lander looking to the south-southwest (175° to 230°) showing measured rocks (circled), the rockier terrain of *Homestead hollow* and the rockier terrain outside the crater. A portion of the afternoon panorama that has been stretched and is not true color.

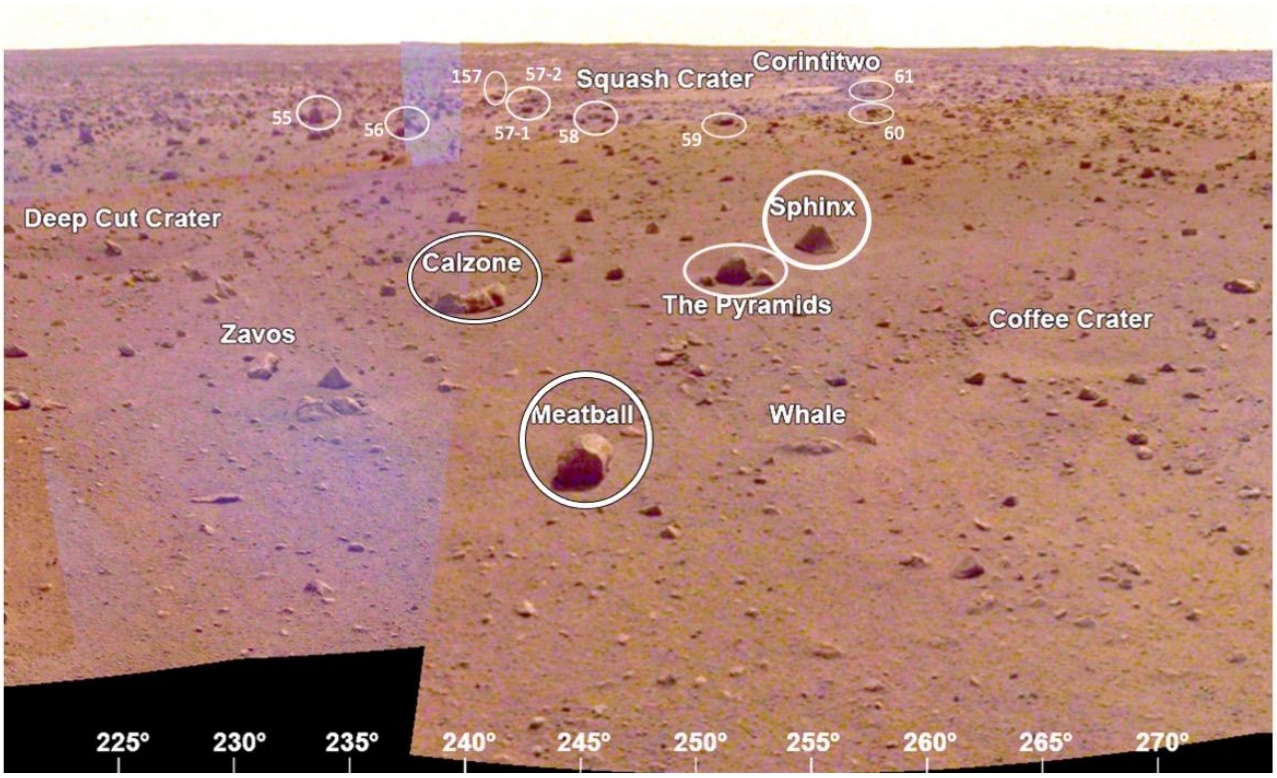

Figure 12. The view from the lander looking to the west-southwest (220° to 275°) showing measured rocks (circled), the rockier terrain of *Homestead hollow* and the indistinct rim. Note Corintitwo crater (a Corinto secondary crater in view, Golombek, Kipp et al., 2017, Golombek, Warner et al., 2020) is about 40 m away. A portion of the afternoon panorama that has been stretched and is not true color.

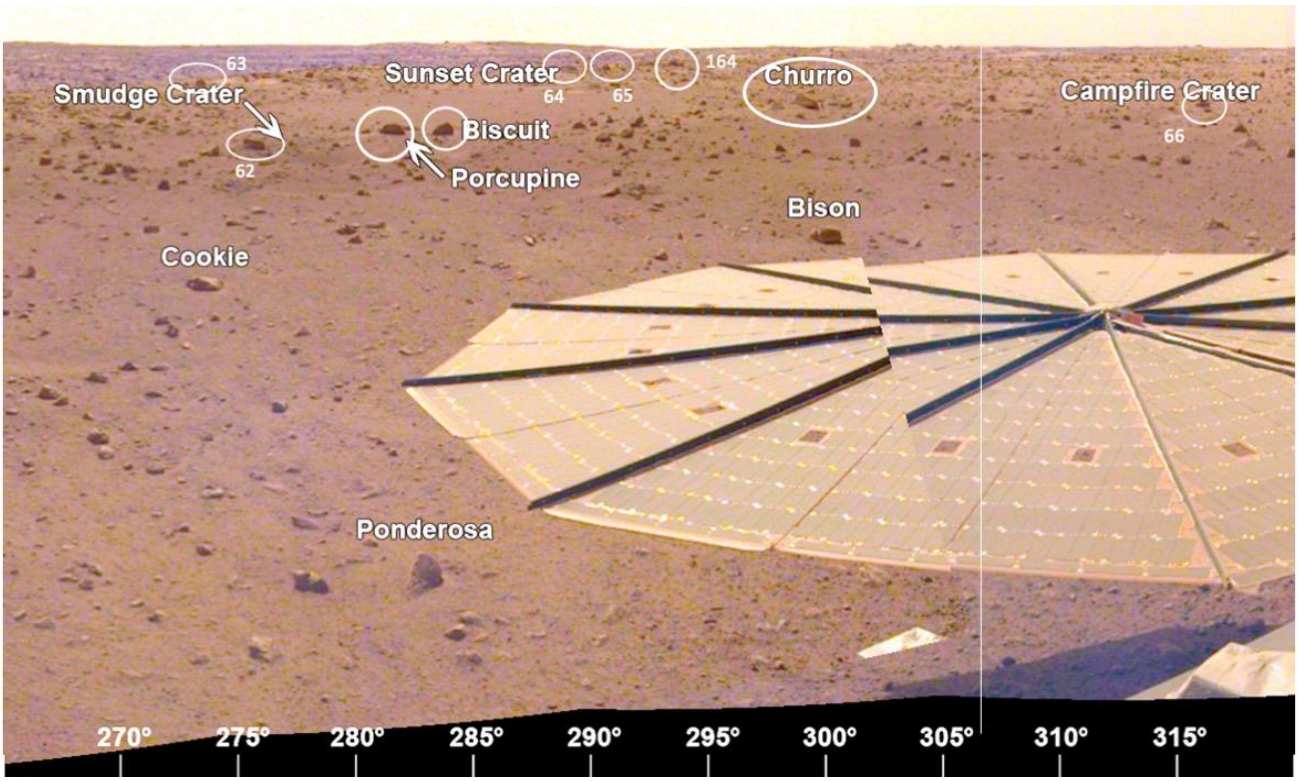

Figure 13. The view from the lander looking to the west-northwest (265° to 320°) showing measured rocks (circled), the solar panel in the foreground and the rockier terrain of western *Homestead hollow*. Note Sunset, Smudge and Campfire craters. A portion of the afternoon panorama that has been stretched and is not true color.

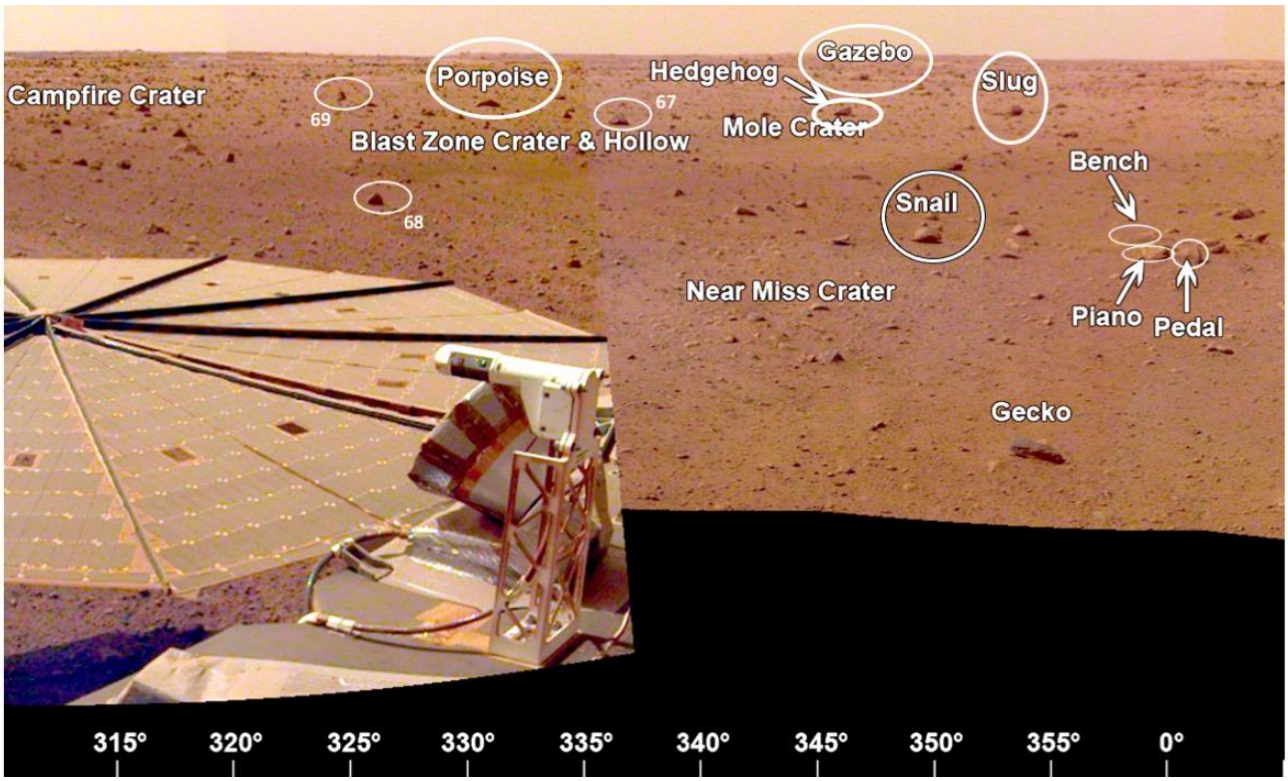

Figure 14. The view from the lander looking to the north-northwest (310° to 0°) showing measured rocks (circled), the solar panel, the rockier terrain of *Homestead hollow*, and several small craters. Also note a meteorology mast. A portion of the afternoon panorama that has been stretched and is not true color.

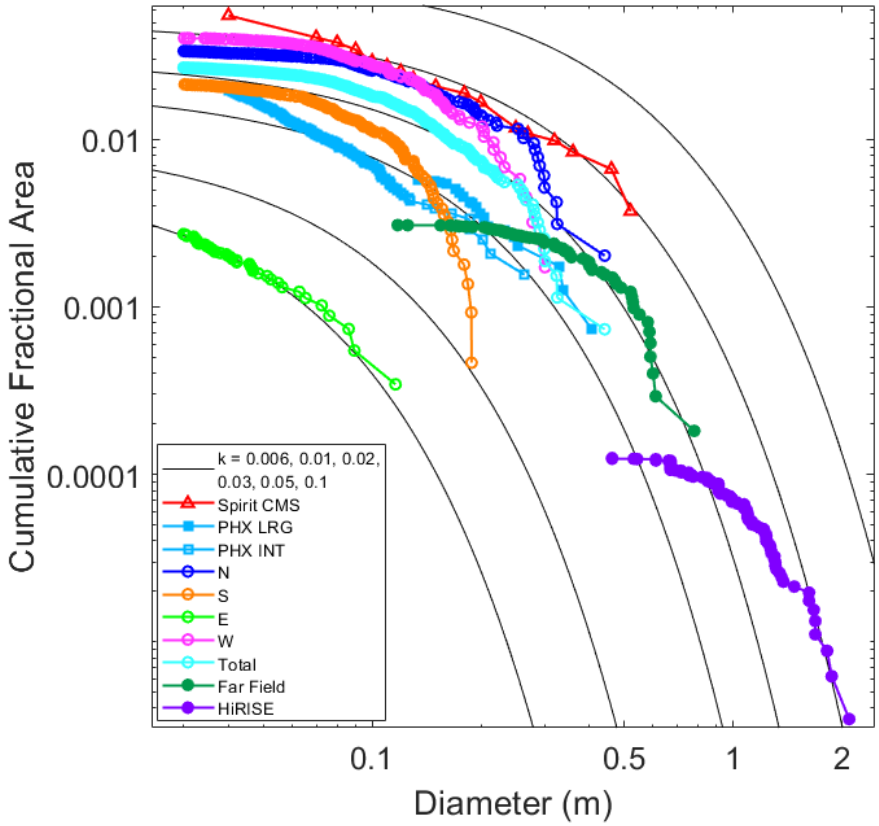

Figure 15. Cumulative fractional area versus diameter plot of rocks around the InSight lander within 10 m (near field), within 40 m (far field) and in HiRISE. Areas within 10 m around the lander are: North (N), South (S), East (E, *Homestead hollow*), West (W) and all areas combined (total). Also shown are the Phoenix (Heet et al., 2009; Golombek, Huertas et al., 2012) and Spirit landing site (Golombek et al., 2006) rocks, rocks detected in HiRISE, and exponential model curves for 0.6%, 1%, 2%, 3%, 5% and 10% rock abundance (Golombek and Rapp, 1997). Confirmed HiRISE rocks measured in a 1 km^2 area around the lander are shown in Figure 17.

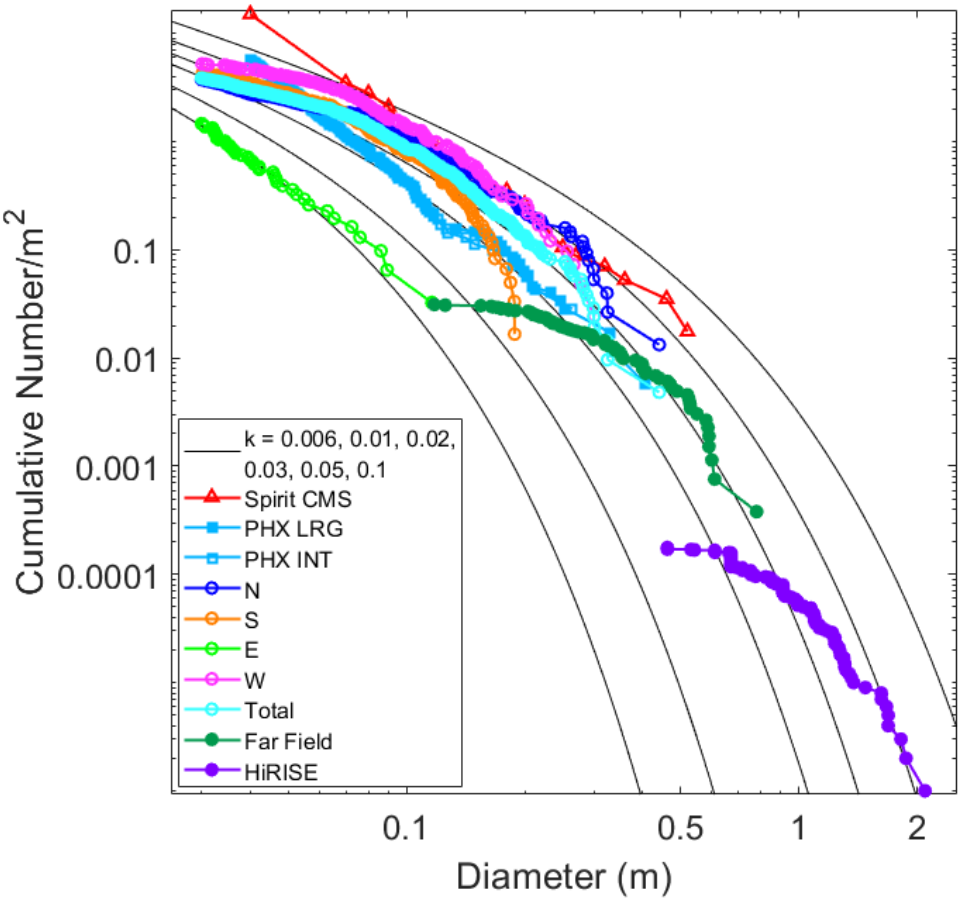

Figure 16. Cumulative number per m^2 versus diameter of rocks within 10 m of the lander (near field), in the far field (within 40 m) and in HiRISE. Also shown are the Phoenix (Heet et al., 2009; Golombek, Huertas et al., 2012) and Spirit landing site (Golombek et al., 2006) rocks, and exponential model curves for 0.6%, 1%, 2%, 3%, 5% and 10% rock abundance (Golombek and Rapp, 1997; Golombek, Haldemann et al., 2003). Confirmed HiRISE rocks that are plotted were measured in a 1 km^2 area around the lander shown in Figure 4.1.

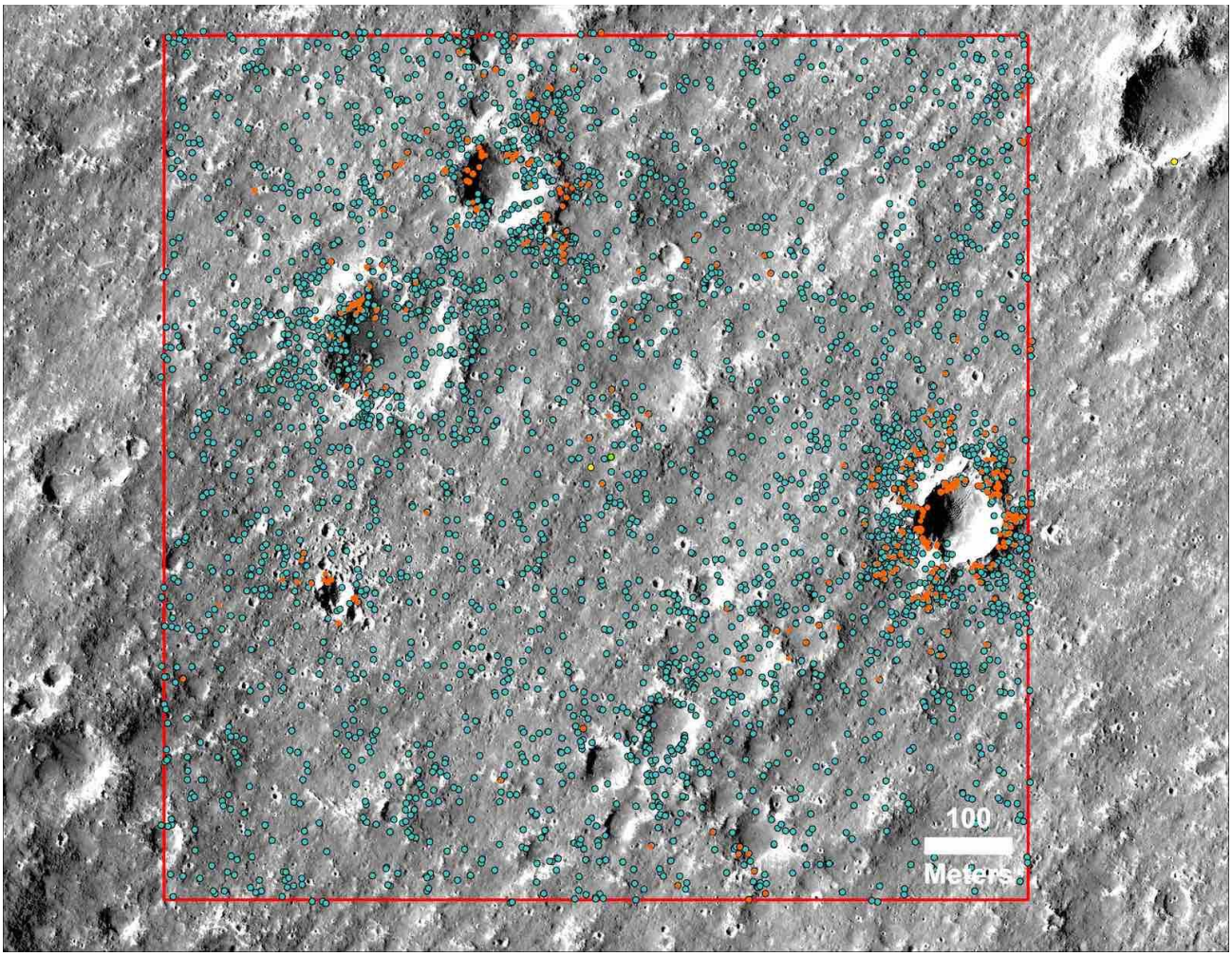

Figure 17. Rocks identified in HiRISE images in 1 km sided square centered on the InSight lander (yellow dot). Blue dots are rocks identified by a human as described in the text. Orange dots are the machine vision detected rocks (Golombek, Kipp et al., 2007; Golombek, Kass et al., 2020) that have been confirmed by a human. Light green rock is Hanging rock (21 m to the northeast at 53° azimuth, measured clockwise from north), that was detected by varying parameters to detect a larger number of rocks. E Pinnacle (60 m to the northeast at 28° azimuth), First (19 m to the southeast at 160° azimuth) and Gazebo (35 m to the northwest at 347° azimuth) rocks are the three orange rocks closest to the lander (see Figure 6 and Table 3). Note rocky ejecta craters with concentrations of rocks.

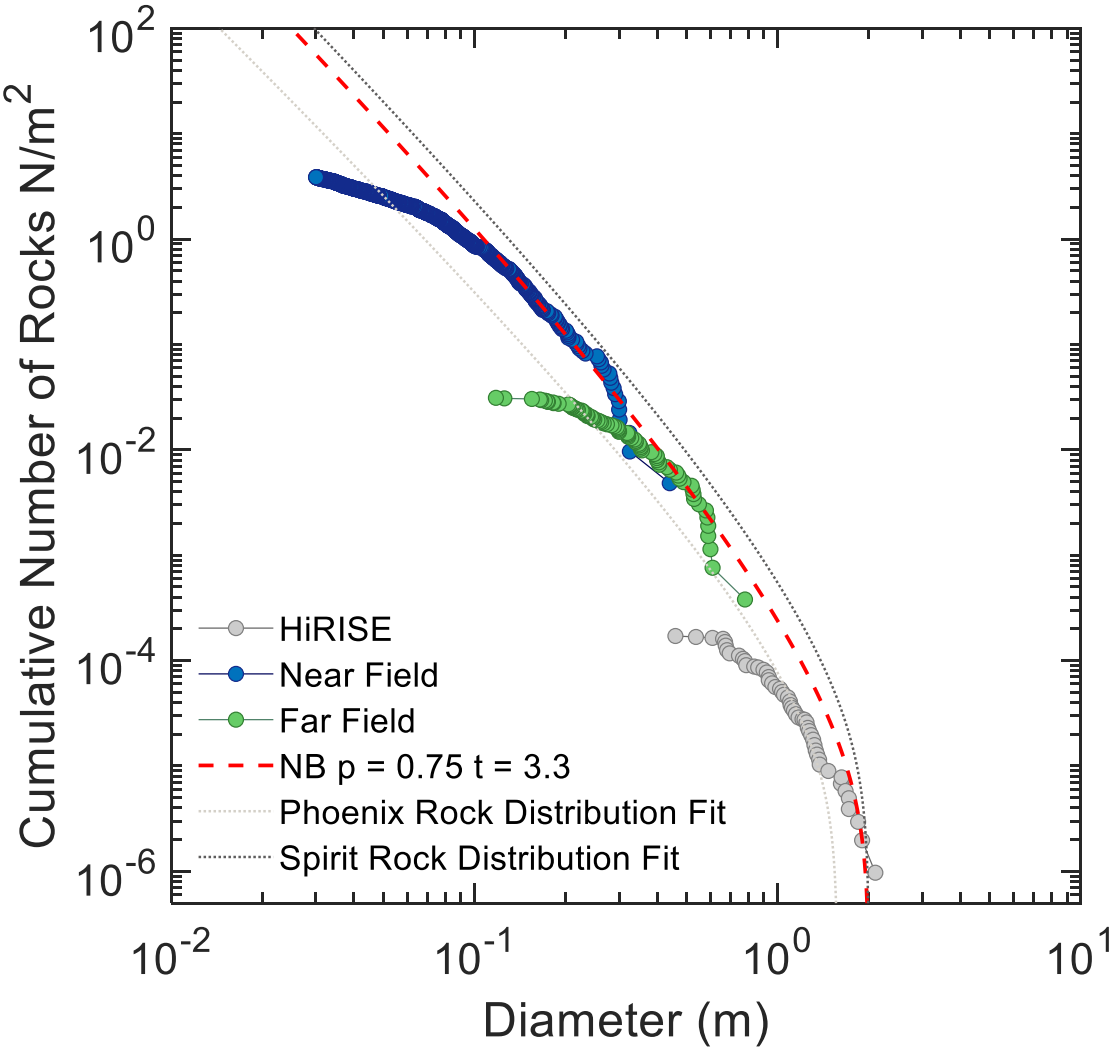

Figure 18. Cumulative number of rocks per m^2 versus diameter for the near and far fields and in HiRISE. Based on the fragmentation model of Charalambous (2014), the red dashed line indicates the NB fit (p = 0.75, t = 3.3) to the compilation of all rock counts measured at InSight. The dotted lines represent the NB fits to the Spirit and Phoenix landing sites (Golombek, Kipp et al., 2017), shown here for comparison.